

Spectropolarimetric characterisation of exoplanet host stars in preparation of the *Ariel* mission

II. The magnetised wind environment of TOI-1860, DS Tuc A, and HD 63433

S. Bellotti^{1,2}, A. Lavail², D. Evensberget^{1,3}, A. A. Vidotto¹, C. Danielski⁴, B. Edwards^{5,6}, G. A. J. Hussain⁷, T. Lüftinger⁷, J. Morin⁸, P. Petit², S. Boro Saikia⁹, G. Micela¹⁰, and A. López Ariste²

¹ Leiden Observatory, Leiden University, PO Box 9513, 2300 RA Leiden, The Netherlands
e-mail: bellotti@strw.leidenuniv.nl

² Institut de Recherche en Astrophysique et Planétologie, Université de Toulouse, CNRS, IRAP/UMR 5277, 14 avenue Edouard Belin, F-31400, Toulouse, France

³ Centre for Planetary Habitability (PHAB), Department for Geosciences, University of Oslo, Oslo, Norway

⁴ INAF - Osservatorio Astrofisico di Arcetri, Largo E. Fermi 5, 50125, Firenze, Italy

⁵ SRON, Netherlands Institute for Space Research, Niels Bohrweg 4, NL-2333 CA, Leiden, The Netherlands

⁶ Department of Physics and Astronomy, University College London, Gower Street, WC1E 6BT London, UK

⁷ Science Engagement and Oversight Office, Directorate of Science, European Space Research and Technology Centre (ESA/ESTEC), Keplerlaan 1, 2201 AZ, Noordwijk, The Netherlands

⁸ Laboratoire Univers et Particules de Montpellier, Université de Montpellier, CNRS, F-34095, Montpellier, France

⁹ University of Vienna, Department of Astrophysics, Türkenschanzstrasse 17, A-1180 Vienna, Austria

¹⁰ INAF - Osservatorio Astronomico di Palermo, Piazza del Parlamento 1, 90134, Palermo, Italy

Received ; accepted

ABSTRACT

Aims. We update the status of the spectropolarimetric campaign dedicated to characterise the magnetic field properties of a sample of known exoplanet-hosting stars included in the current target list of the *Ariel* mission. The main aims are to inform observing strategies and subsequent analysis of the data of the *Ariel* mission, and to provide background information on the magnetic properties of the target and their variability on timescales of at least a few years.

Methods. We analysed spectropolarimetric data collected for 15 G-M type stars with Neo-Narval, HARPSpol, and SPIRou to assess the detectability of the large-scale magnetic field. For three stars we reconstructed the magnetic field topology and its temporal evolution via Zeeman-Doppler imaging (ZDI). Such reconstructions were then used to perform three-dimensional magnetohydrodynamical simulations of the stellar wind and environment impinging on the hosted exoplanets.

Results. We detected the magnetic field of six stars. Of these, we performed ZDI reconstructions for the first time of TOI-1860 and DS Tuc A, and for the second time of HD 63433, providing temporal information of its large-scale magnetic field. Consistently with previous results on young ($\sim 50 - 100$ Myr) solar-like stars, the large-scale magnetic field is moderately strong (30-60 G on average) and complex, with a significant fraction of magnetic energy in the toroidal component and high-order poloidal components. From the simulations of the stellar wind, we found the orbit of TOI-1860 b to be almost completely sub-Alfvénic, the orbits of DS Tuc A b and HD 63433 d to be trans-Alfvénic, and the orbits of HD 63433 b and c to be super-Alfvénic. We obtained marginal detections of the magnetic field for TOI-836 and TOI-2076, and detections for TOI-1136, but the number of observations is not sufficient for magnetic mapping.

Conclusions. A magnetic star-planet connection can occur for most of TOI-1860 b's orbit. This can happen more sporadically for DS Tuc A b and HD 63433 c given the lower fraction of their orbit in the sub-Alfvénic regime. The orbit of HD 63433 c is nevertheless more sub-Alfvénic than previously simulated owing to the temporal evolution of the stellar magnetic field. For HD 63433 b and c, we expect the formation of a bow shock between the stellar wind and the planet despite the evolution of the stellar magnetic field.

Key words. Stars: magnetic field – Stars: activity – Techniques: polarimetric

1. Introduction

Ariel is a medium-class (M4) science mission of the European Space Agency planned to be launched in 2029 (Tinetti et al. 2018, 2022). The aim of *Ariel* is to perform a comprehensive survey of the chemical composition and structure of exoplanetary atmospheres, in order to understand exoplanets' bulk composition and how planetary systems form and evolve. The mission will target about a thousand transiting planets orbiting different

types of host stars, from early A type to late M (Zingales et al. 2018; Edwards et al. 2019; Edwards & Tinetti 2022)¹.

To perform an informed target selection and optimise the observing strategy of *Ariel*, it is important to characterise exoplanet-hosting stars in a homogeneous manner (Danielski et al. 2022; Magrini et al. 2022). This is also crucial to prevent a biased interpretation of the planetary atmosphere and chemistry.

¹ The mission candidate sample is available here: https://github.com/arielmision-space/Mission_Candidate_Sample

Stellar magnetic activity is a known source of uncertainty in differential spectroscopy analyses (Pont et al. 2007, 2013), because it can alter the stellar spectrum on the timescale of the transit (Spina et al. 2020). Magnetically induced inhomogeneities on stellar surfaces hinder the precise measurement of both the planetary radius and mass, therefore affecting the atmospheric scale height estimate and the subsequent retrieval (Oshagh et al. 2013; Changeat et al. 2020; Di Maio et al. 2023). Depending on the coverage and global configuration of these magnetic inhomogeneities, ambiguous atomic and molecular absorption and emission features can occur (e.g. Rackham et al. 2018, 2019; Salz et al. 2018; Genest et al. 2022). Moreover, the magnetic field of stars governs the amount of short-wavelength radiation (such as extreme ultraviolet and X-rays Güdel 2004; Reiners et al. 2022) and stellar wind impinging on planets (e.g. Vidotto et al. 2015; Garraffo et al. 2016; Alvarado-Gómez et al. 2022), ultimately regulating photochemistry (e.g. Locci et al. 2022, 2024) and the erosion of planetary atmospheres (e.g. Lammer et al. 2003; Lanza 2013; McCann et al. 2019; Carolan et al. 2021a; Hazra et al. 2020; Presa et al. 2024; Van Looveren et al. 2025).

In this paper, we update the status of the spectropolarimetric survey aimed at characterising the stellar magnetic field properties and surrounding environment of a representative sample of stars in the current list of potential *Ariel* targets (Edwards et al. 2019; Edwards & Tinetti 2022). The work of Bellotti et al. (2024) introduced such a survey and focussed on the solar-type star HD 63433. With the information on the stellar large-scale magnetic field at hand, stellar wind simulations have shown that young active stars could produce wind conditions that are harsher compared to the present solar neighbourhood (see Vidotto et al. 2012; Nicholson et al. 2016; Folsom et al. 2020; Vidotto et al. 2023, for a few examples). Being dictated by the stellar magnetic field, the environment varies over time in correlation with the stellar magnetic cycle (McComas 2003, Smith et al. in review) and the evolution of the star (e.g. Johnstone et al. 2021). As a result, the region of space in which specific magnetic star-planet interactions take place could be temporarily modified, altering both the nature and intensity of these interactions.

Our survey is divided into three steps (see also Bellotti et al. 2024): 1) a snapshot campaign to assess the detectability of the large-scale magnetic field and optimise further observations, 2) an observing campaign to reconstruct the topology of the surface's stellar magnetic field, and 3) a long-term monitoring to constrain the evolution and variability of the field. The work presented in this paper addresses all of these steps for new targets with respect to Bellotti et al. (2024). We first describe the snapshot polarimetric observations aimed at determining which stars are suitable for spectropolarimetric follow-up. Then we present the first large-scale magnetic field reconstructions via Zeeman-Doppler imaging (ZDI; Semel 1989; Donati et al. 1997) for TOI-1860 and DS Tuc A. Finally, we provide a new ZDI reconstruction for HD 63433. The large-scale magnetic field topology of this star was previously reconstructed by Bellotti et al. (2024), and hence we analyse its temporal evolution over a timescale of a year.

This paper is structured as follows. In Sect. 2, we describe the target selection for this study and the spectropolarimetric observations and in Sect. 3 we analyse the detectability of the large-scale magnetic field. In Sect. 4, we focus on the reconstruction of the large-scale magnetic field of TOI-1860, DS Tuc A, and HD 63433 and in Sect. 5 we describe the magnetohydrodynamical simulations of the environment around these stars. We finally discuss our results and draw our conclusions in Sect. 6.

2. Observations

2.1. Target selection

The construction of the current *Ariel* target list is described in Edwards et al. (2019), Mugnai et al. (2020), and Edwards & Tinetti (2022). It contains 748 exoplanet systems whose host stars have a spectral type ranging from A ($T_{\text{eff}} \sim 10\,000$ K) to late M ($T_{\text{eff}} \sim 2600$ K). Starting from this list, we applied a series of selection criteria to obtain a sample of stars whose properties are supposedly suitable for magnetometry. The stars should: i) be bright enough in order to carry out observations with a reasonable exposure time and obtain a moderate signal-to-noise ratio (S/N), and ii) exhibit a certain level of magnetic activity as quantified by specific proxies. The latter point would then translate into a potentially detectable large-scale magnetic field.

We applied the following quantitative selection criteria:

- Stellar mass $M_* < 1.2 M_{\odot}$. The outer convective envelopes typical of these type of stars are known to produce persistent and intense magnetic fields via dynamo (e.g. Schrijver & Zwaan 2000).
- Rotation period $P_{\text{rot}} < 30$ d, equatorial velocity $v_{\text{eq}} \sin i > 2 \text{ km s}^{-1}$, and chromospheric activity $S\text{-index} > 0.2$ (or $\log R'_{\text{HK}} > -4.8$). These selection limits, corresponding to fast rotation and high magnetic activity, translate into magnetic detection fractions larger than 70% according to the results of the Bcool snapshot survey (Marsden et al. 2014).
- Magnitude in H or V band lower than 9.0. This threshold is applied to limit a polarimetric exposure to a maximum of approximately one hour for spectropolarimeters operating at optical or near-infrared wavelengths.

We applied conservative activity thresholds to search for the most active stars in the current list of *Ariel* targets. Although HD 63935 and HD 89345 have $v_{\text{eq}} \sin i < 2 \text{ km s}^{-1}$, we kept them in our list because of their brightness. We also kept HD 260655 albeit its rotation period is 37.5 d because Lehmann et al. (2024) recently showed that slowly rotating ($P_{\text{rot}} \sim 100$ d) M dwarfs are capable of generating strong magnetic fields. In general, our selection criteria include the mass dependency of the rotation-activity relation (e.g. Pizzolato et al. 2003), but indirectly, since other factors such as brightness dominate our shortlisting. Indeed, most of the M dwarfs in the *Ariel* Candidate Sample are too faint to be efficiently observed with spectropolarimetry, regardless of their rotation period or activity level. Finally, we did not select stars that have a spectropolarimetric characterisation already, such as GJ 436 (Bellotti et al. 2023a; Vidotto et al. 2023) and AU Mic (Klein et al. 2021; Donati et al. 2023) for instance.

The stellar sample analysed in this work contains 15 objects and its properties are listed in Table 1. The fraction of low-mass, highly-to-moderately active stars in the *Ariel* Candidate Sample that are shortlisted with our selection criteria excluding the magnitude criterion is $\sim 30\%$. Our 15 stars are therefore representative of the bright end of this specific parameter space. We note that for $\log R'_{\text{HK}}$ we are currently using literature values, but that in the future publications we will use homogeneous data that are currently being prepared by Wizani et al, in prep. We also note that the list of targets for *Ariel* is being optimised over time, hence some of the targets selected for this spectropolarimetric campaign may have been removed from the mission candidate sample, but they remain interesting targets (e.g. for other follow-up efforts than *Ariel*).

Table 1. Properties of the selected stars.

Star	RA	DEC	SpT	Mass [M_{\odot}]	H	V	P_{rot} [d]	$v_{\text{eq}} \sin(i)$ [km s^{-1}]	S-index	$\log R'_{\text{HK}}$	N_{pl}
HD 63433	07 49 55.06	+27 21 47.46	G5	0.99	5.36	6.92	6.5 ^a	7.3 ^a	...	-4.36 ^b	3
HD 63935	07 51 41.99	+09 23 09.79	G5	0.97	6.96	8.58	...	0.3 ^c	2
HD 89345	10 18 41.06	+10 07 44.50	G5	1.18	7.77	9.38	...	0.1 ^c	1
HD 152843	16 55 08.36	+20 29 28.79	G0	1.06	7.66	8.86	...	7.5 ^c	2
HD 158259	17 25 24.10	+52 47 26.47	G0	1.03	5.03	6.48	20.0 ^d	1.6 ^c	0.19 ^e	-4.75 ^e	5
HD 260655	06 37 10.80	+17 33 53.33	M0	0.44	6.03	9.59	37.5 ^f	< 2.0 ^f	0.92 ^e	-4.84 ^e	2
HAT-P-22	10 22 43.59	+50 07 42.06	G5	1.13	7.94	9.76	28.7 ^g	1.65 ^g	0.15 ^e	-5.09 ^e	1
DS Tuc A	23 39 39.48	-69 11 44.71	G5	1.01	6.76	8.23	2.85 ^h	17.8 ^h	0.88 ^e	-4.06 ^e	1
Kepler-444	19 19 00.55	+41 38 04.58	K0	0.67	6.77	8.87	17.2 ⁱ	5
K2-116	22 24 36.38	-11 34 43.30	K7	0.69	8.02	10.80	29.8 ^j	1
TOI-836	15 00 19.40	-24 27 14.69	K4	0.68	6.98	9.92	21.99 ^k	1.9 ^k	1.31 ^e	-4.44 ^e	2
TOI-1136	12 48 44.37	+64 51 19.15	G5	1.02	8.09	9.53	8.19 ^l	6.7 ^m	0.32 ^m	-4.49 ^m	6
TOI-1860	15 05 49.90	+64 02 49.94	G5	0.99	6.88	8.40	4.43 ⁿ	10.4 ⁿ	...	-4.25 ⁿ	1
TOI-2076	14 29 34.24	+39 47 25.54	K1	0.82	7.19	9.14	6.84 ^o	5.7 ^p	...	-4.37 ^o	3
Wolf 503	13 47 23.44	-06 08 12.73	K3.5	0.63	7.77	10.30	...	2.8 ^c	1

Notes. The columns are: identifier, right ascension and declination (J2000), spectral type, stellar mass, H band magnitude, V band magnitude, rotation period, projected equatorial velocity, S-index, chromospheric activity index, and number of exoplanets. The information is primarily extracted from the *Ariel* stellar catalogue (Danielski et al. 2022) available at <https://sites.google.com/inaf.it/ariellstellarcatalogue/>. References: *a.* Mann et al. (2020) *b.* Marsden et al. (2014), *c.* Tsantaki et al. (2025), *d.* Hara et al. (2020), *e.* Boro Saikia et al. (2018), *f.* Luque et al. (2022), *g.* Mancini et al. (2018), *h.* Newton et al. (2019), *i.* Angus et al. (2018), but Mazeh et al. (2015) reported a rotation period of 49.4 d instead, *j.* Reinhold & Hekker (2020), *k.* Hawthorn et al. (2023), *l.* Canto Martins et al. (2020), *m.* Dai et al. (2023), *n.* Giacalone et al. (2022), *o.* Osborn et al. (2022) and Frazier et al. (2023) reported a rotation period of 7.12 d, and *p.* Frazier et al. (2023).

2.2. Instruments

We analysed spectropolarimetric observations collected with Neo-Narval, HARPSpol, and SPIRou. The journal of the observations can be found in Table B.1, excluding the 2023 observations of HD 63433 published in Bellotti et al. (2024).

Neo-Narval² is the upgraded version of Narval (López Ariste et al. 2022) mounted on the 2 m Telescope Bernard Lyot (TBL) at the Pic du Midi Observatory in France (Donati 2003). The upgrade occurred in 2019, and kept the main performances of Narval: a spectral coverage from 380 to 1050 nm, and a median spectral resolving power of $\sim 65\,000$ after data reduction (López Ariste et al. 2022).

HARPSpol³ (Snik et al. 2011; Piskunov et al. 2011) is the spectropolarimeter for the HARPS spectrograph (Mayor et al. 2003) mounted at the Cassegrain focus of the ESO 3.6 m telescope at La Silla observatory, Chile. HARPSpol observations cover the wavelength range between 380 and 691 nm with a 8 nm gap at 529 nm separating the red and blue detectors. The resolving power is $R \sim 110\,000$. The data reduction was carried out with the PyReduce package⁴ (Piskunov et al. 2021), the updated implementation in python of the versatile REDUCE package (Piskunov & Valenti 2002). The reduction with PyReduce is run with a series of standard steps, similar to REDUCE as described by Rusomarov et al. (2013). For more information on the steps applied to our observations see Bellotti et al. (2024).

The SpectroPolarimètre InfraRouge (SPIRou⁵) is the near-infrared spectropolarimeter mounted at Cassegrain focus on the 3.6 m CFHT atop Maunakea, Hawaii (Donati et al. 2020). The instrument allows linear and circular polarisation observations

at a spectral resolving power of $R \sim 70\,000$ for a wavelength coverage between 960 to 2500 nm (*YJHK* bands). Optimal extraction of SPIRou spectra was carried out with *A Pipeline to Reduce Observations* (APER0 v0.6.132), a fully automatic reduction package installed at CFHT (Cook et al. 2022).

Our observations were carried out in circular polarisation mode. The output consists of unpolarised (Stokes *I*), circularly polarised (Stokes *V*) and null (Stokes *N*) high-resolution spectra. The Stokes *N* spectrum is practical to check the presence of spurious polarisation signatures or data reduction issues (see Donati et al. 1997; Bagnulo et al. 2009; Tessore et al. 2017, for more details).

3. Magnetic field detectability

3.1. Least-squares deconvolution

For the first part of our campaign dedicated to the detectability of the large-scale magnetic field, we requested a handful of observations per star at separated days throughout the observing semester. We applied least-squares deconvolution (LSD; Donati et al. 1997; Kochukhov et al. 2010) to the collected unpolarised, circularly polarised and null spectra. We used the `pylsd` python code⁶ which is part of the `specpolflow` package (Folsom et al. 2025) to deconvolve the spectra with a synthetic atomic line list. Together with wavelength, a line list typically contains the associated atomic number, depth, excitation potential, and effective Landé factor (indicated as g_{eff}), which encapsulates the sensitivity to Zeeman effect. The deconvolution results in a single, high-signal-to-noise ratio (S/N) kernel (for Stokes *I*, *V*, and *N*) summarising the properties of hundreds or thousands of spectral lines.

⁶ available at <https://github.com/folsomcp/LSDpy>

² <https://www.news.obs-mip.fr/neo-narval-pic-du-midi/>

³ <https://www.eso.org/sci/facilities/lasilla/instruments/harps.html>

⁴ <https://github.com/AWehrhahn/PyReduce>

⁵ <https://www.cfht.hawaii.edu/Instruments/SPIRou/>

Table 2. Properties of the synthetic line lists.

Name	Instrument	N _{obs}	Mask	$\langle\lambda\rangle$ [nm]	$\langle g_{\text{eff}}\rangle$	N _{lines}
HD 63433	Neo-Narval	9	5500_4.5	447	1.23	3826
HD 63935	Neo-Narval	4	5500_4.5	447	1.23	3827
HD 63935	HARPSpol	4	5500_4.5	447	1.23	3682
HD 89345	Neo-Narval	5	5500_4.0	440	1.21	5167
HD 152843	Neo-Narval	3	6250_4.0	430	1.21	3401
HD 158259	Neo-Narval	3	5750_4.5	440	1.23	3309
HD 260655	SPIRou	1	4000_5.0	1680	1.25	2432
HAT-P-22	Neo-Narval	2	5500_4.5	447	1.23	3826
DS Tuc A	HARPSpol	10	5500_4.5	447	1.23	3702
Kepler-444	Neo-Narval	4	5000_4.5	443	1.22	6046
K2-116	SPIRou	3	4500_4.5	1700	1.24	3868
TOI-836	SPIRou	1	4500_4.5	1700	1.24	3764
TOI-1136	Neo-Narval	6	5750_4.5	440	1.23	3311
TOI-1860	Neo-Narval	20	5750_4.5	440	1.23	3313
TOI-2076	Neo-Narval	6	5000_4.5	443	1.22	6046
Wolf 503	SPIRou	3	4500_4.5	1700	1.24	3905

Notes. The columns indicate: identifier of the star, instrument used for the observations, number of observations, properties of the line list in the form $T_{\text{eff}}[\text{K}]_{\text{logarithm}}$ surface gravity[cm s^{-1}], number of lines used in LSD, average wavelength of the mask, and average effective Landé factor of the mask. The lower number of lines used for HARPSpol stems from the narrower wavelength coverage compared to Neo-Narval. For HD 63433, the values refer to the observations taken in 2024 (see also Table B.1).

We generated synthetic line lists via the Vienna Atomic Line Database⁷ (VALD, Ryabchikova et al. 2015), selecting models whose effective temperature and surface gravity are close to the values reported in the *Ariel* stellar group catalogue for each target. For observations at optical wavelengths with Neo-Narval and HARPSpol, we chose atomic lines between 350 and 1097 nm, with known g_{eff} , and whose depth relative to the continuum is larger than 40% (following Moutou et al. 2007). We adopted an LSD normalisation wavelength of 700 nm and a normalisation g_{eff} of 1.2. For observations at near-infrared wavelengths with SPIRou, we selected atomic lines between 950 and 2600 nm, with known g_{eff} , and with a relative depth larger than 3% (see e.g. Bellotti et al. 2023b). In this case we adopted a normalisation wavelength of 1700 nm and a normalisation Landé factor of 1.2.

The properties of the synthetic line lists used in this work are summarised in Table 2, in which we also report the total number of spectropolarimetric observations. To quantify whether a circularly polarised Zeeman signature is detected, and thus the large-scale magnetic field, we computed the false-alarm probability (FAP; see Donati et al. 1997, for more details). A successful detection corresponds to $\text{FAP} < 10^{-4}$, and a marginal detection to $\text{FAP} = 10^{-2} - 10^{-4}$. The same metric is applied to Stokes N in order to check for spurious polarisation signatures. The results are listed in Table B.1.

Zeeman signatures in circular polarisation are detected for TOI-1136, TOI-1860, and DS Tuc A, as well as for the newest observations of HD 63433. As a result, these stars are amenable to magnetic field characterisation. For TOI-836 we obtained one marginal detection and for TOI-2076 we obtained two while the remaining four observations are non-detections. While for TOI-836, TOI-1136, and TOI-2076 we require additional observa-

tions for producing a ZDI map, for TOI-1860, HD 63433, and DS Tuc A we collected a number of observations that sample various longitudes and are sufficient for the ZDI reconstruction (see Sect. 4).

We did not detect circularly polarised Zeeman signatures in eight stars over multiple snapshot observations. This is not completely surprising as exoplanets are more easily detected around magnetically inactive stars, that is with a weak large-scale magnetic field. Another possibility is that the large-scale configuration of these stars is such that the magnetic polarity cancellation is substantial, although distributing multiple observations across the semester should allow for some detections owing to stellar rotation and magnetic field variability. This aspect makes the substantial polarity cancellation scenario less likely. The number of non-detections of our stars are overall in agreement with the statistics of the BCool campaign (Marsden et al. 2014), for which a moderate fraction of the large-scale magnetic field of stars with surface temperature between 5250 K and 6000 K (that is, spectral types G5 to G0) is not detected. This is also noted considering the stellar rotation period, since most of our non-detections are for slowly rotating stars with $P_{\text{rot}} > 20$ d.

3.2. Longitudinal magnetic field

The longitudinal magnetic field is the net, line-of-sight-projected component of the large-scale magnetic field (e.g. Donati et al. 1997). We used the general formula as in Cotton et al. (2019),

$$B_l = \frac{h}{\mu_B \lambda_0 g_{\text{eff}}} \frac{\int v V(v) dv}{\int (I_c - I(v)) dv}, \quad (1)$$

where λ_0 and g_{eff} are the normalisation wavelength and Landé factor of the LSD profiles, I_c is the continuum level, v is the radial velocity associated to a point in the spectral line profile in the star's rest frame, h is the Planck's constant and μ_B is the Bohr magneton. To express it as in Rees & Semel (1979) and Donati et al. (1997), one can use $hc/\mu_B = 0.0214 \text{ Tm}$, where c is the speed of light in m s^{-1} .

We computed the longitudinal magnetic field (B_l) for TOI-836, TOI-1136, TOI-1860, TOI-2076, HD 63433, and DS Tuc A using the continuum-normalised Stokes profiles. In practice, we fitted a linear model to the region outside the Stokes I LSD profile, to include residuals of continuum normalisation at the level of the spectra, and we re-scaled the Stokes V LSD profiles by the same fit. For TOI-1136 and TOI-2076, we used only the observations in which Stokes N detection is at most marginal. For the stars without detections, we computed 3σ upper limits. The results are given in Table B.1.

For TOI-1136, the integral range was set to $\pm 15 \text{ km s}^{-1}$. For the two observations when Stokes V was marginally and completely detected and Stokes N showed only a marginal detection (18 and 19 March 2024), we obtained $25 \pm 44 \text{ G}$ and $131 \pm 60 \text{ G}$, where the error bar indicates the 1σ formal uncertainty. We caution that the presence of a marginal detection in Stokes N can alter the polarisation signature in Stokes V , ultimately affecting the value of B_l . For TOI-2076 we integrated Eq. 1 between $\pm 20 \text{ km s}^{-1}$ and obtained $-75 \pm 17 \text{ G}$ and $69 \pm 34 \text{ G}$.

For TOI-1860, the integral range was set to $\pm 25 \text{ km s}^{-1}$. For the observations in 2024 with a detection, we found values between -5 G and 19 G and for the 2025 observations we found values between -21 G and 20 G . For DS Tuc A, we used a range of $\pm 35 \text{ km s}^{-1}$ and obtained values between -36 G and -4 G , with an average of -19 G . For HD 63433, we applied Eq. 1 between $\pm 20 \text{ km s}^{-1}$ from the line centre at -15.9 km s^{-1} . We found

⁷ <http://vald.astro.uu.se/>

values between -6 G and 5 G, with an average of -1.0 G, similar to the measurements on the 2023 data (Bellotti et al. 2024).

4. Large-scale magnetic field reconstruction

The second and third parts of our spectropolarimetric campaign are dedicated to reconstructing the stellar large-scale magnetic field for the first time or across different epochs. So far, we have performed enough monitoring to reconstruct a ZDI map for TOI-1860, DS Tuc A, and HD 63433. For TOI-1860, we only used the June and July 2025 data set, since the August 2025 data yielded non-detections and the 2024 data set did not have enough observations. The ZDI algorithm inverts a time series of Stokes V LSD profiles into a magnetic field map, by iteratively synthesising and adjusting model Stokes V profiles, until a maximum-entropy solution at a fixed reduced χ^2 is achieved (for more information, see Skilling & Bryan 1984; Donati & Brown 1997; Folsom et al. 2018). The field is formally described as the sum of a poloidal and toroidal component, which are both expressed via spherical harmonic decomposition (Donati et al. 2006; Lehmann & Donati 2022). The odd and even spherical harmonics modes are weighted equally in the reconstruction. We employed the `zdi.py` code described in Folsom et al. (2018).

We adopted the weak-field approximation because local field strengths are lower than 160 G for our targets (see Table 3), that is, within the range of applicability of the approximation (typically less 1 kG Kochukhov et al. 2010). We note that magnetic field strengths at unresolved spatial scales are most likely larger than 1 kG as corroborated by Zeeman broadening and intensification measurements (see Kochukhov et al. 2020; Hahlin et al. 2023, for some recent results). Assuming weak-field approximation, Stokes V is proportional to the derivative of Stokes I with respect to wavelength (e.g. Landi Degl’Innocenti 1992). The unpolarised line profiles in each cell of the stellar grid are modelled with a Voigt kernel, parametrised by the line depth (d), Gaussian width (w_G), and Lorentzian width (w_L). The optimal values of these three parameters are obtained with a χ_r^2 minimisation between the median of the observed Stokes I LSD profiles and its model over a grid of (d , w_G , w_L) values. We provide the optimal values for each star below.

The stellar input parameters of ZDI are the rotation period P_{rot} , the projected equatorial velocity $v_{\text{eq}} \sin(i)$, and the inclination i (that is, the viewing angle). Furthermore, the `ZDIpy` code includes surface shear as a function of colatitude (θ) expressed in the form

$$\Omega(\theta) = \Omega_{\text{eq}} - d\Omega \sin^2(\theta), \quad (2)$$

where $\Omega_{\text{eq}} = 2\pi/P_{\text{rot}}$ is the rotational frequency at equator and $d\Omega$ is the differential rotation rate in rad d^{-1} . The variable $d\Omega$ is also an input parameter of ZDI.

The input $v_{\text{eq}} \sin(i)$ used for TOI-1860, DS Tuc A, and HD 63433 is listed in Table 1. The stellar inclination was estimated comparing the stellar radius provided in the stellar working group catalogue with the projected radius $R \sin i = P_{\text{rot}} v_{\text{eq}} \sin i / 50.59$, where $R \sin(i)$ is measured in solar radii, P_{rot} in d, and $v_{\text{eq}} \sin i$ in km s^{-1} . We estimated $i \approx 90^\circ$ for DS Tuc A and TOI-1860, so we adopted a value of $i = 80^\circ$ in ZDI to prevent mirroring effects between the northern and southern hemispheres that a value of 90° would incur. For HD 63433, we used $i = 70^\circ$ as constrained by Mann et al. (2020).

For the latitudinal differential rotation, we performed the parameter optimisation outlined in Donati et al. (2000) and Petit

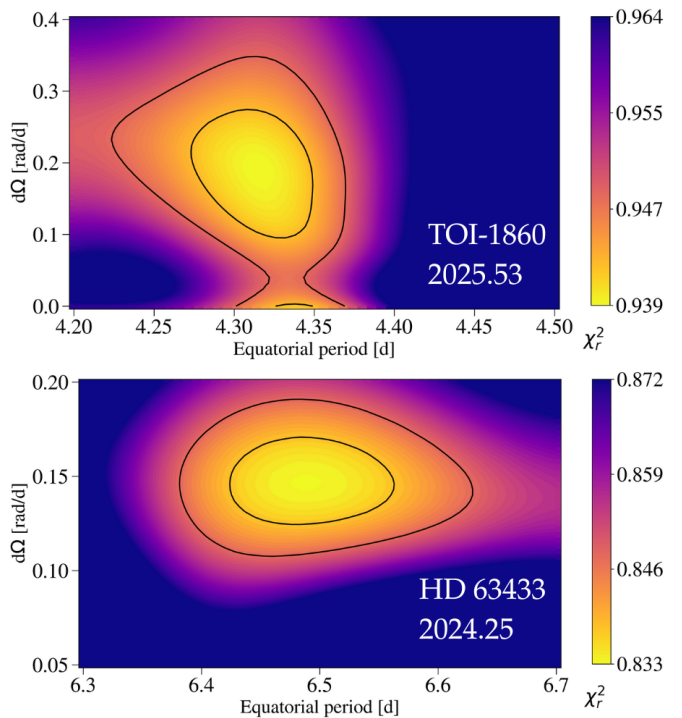


Fig. 1. Joint search of differential rotation and equatorial rotation period for TOI-1860 (top) and HD 63433 (bottom). The panels illustrate the χ_r^2 landscape over a grid of ($P_{\text{rot,eq}}, d\Omega$) pairs, with the 1σ and 3σ contours. The best values are obtained by fitting a 2D paraboloid around the minimum, while their error bars are estimated from the projection of the 1σ contour on the respective axis (Press et al. 1992).

et al. (2002). We generated a grid of ($P_{\text{rot}}, d\Omega$) pairs, reconstructed a ZDI map for each of the pairs, and searched for the values that minimised the χ_r^2 distribution between observations and synthetic LSD profiles, at a fixed entropy level. The best parameters are measured by fitting a 2D paraboloid to the χ_r^2 distribution, and the error bars are obtained from a variation of $\Delta\chi_r^2 = 1$ away from the minimum (Press et al. 1992; Petit et al. 2002). If no differential rotation is constraint, we assumed solid body rotation with P_{rot} from Table 1.

In general, a faster rotation (that is, larger $v_{\text{eq}} \sin(i)$) translates into a decreased polarity cancellation because the Zeeman signatures are more separated in radial velocity space (see Hussain et al. 2009, for example). For this reason, we set the maximum degree of spherical harmonic coefficients ℓ_{max} to 10 for every ZDI reconstruction. We note that a lower value could have been used, since most of the magnetic energy is stored in the $\ell < 6$ degrees. Finally, we fixed the V-band limb darkening coefficient to 0.6964 (Claret & Bloemen 2011).

For each of the three stars, the observations were phased with the following ephemeris

$$\text{HJD} = \text{HJD}_0 + P_{\text{rot}} n_{\text{cyc}}, \quad (3)$$

where P_{rot} is the stellar rotation period and n_{cyc} is the rotation cycle. The reference heliocentric Julian date HJD_0 is the first observation or the median observation, depending on whether solid body rotation or differential rotation was assumed.

4.1. TOI-1860

As reported in Table 1, TOI-1860 has a rotation period of 4.43 d and $v_{\text{eq}} \sin(i) = 10.4 \text{ km s}^{-1}$ (Giacalone et al. 2022). The opti-

Table 3. Properties of the large-scale magnetic field and wind of the studied stars.

Star	$\langle B_V \rangle$ [G]	$ B_{V,\max} $ [G]	$\langle B_V^2 \rangle$ [G ²]	f_{pol} [%]	f_{tor} [%]	f_{dip} [%]	f_{quad} [%]	f_{oct} [%]	$f_{\ell=4}$ [%]	f_{axi} [%]	$f_{\text{axi,pol}}$ [%]	$f_{\text{axi,tor}}$ [%]	\dot{M} [M _⊙ /yr]	\dot{J} [erg]
TOI-1860	37	103	1.8×10^3	28	72	28	13	26	20	73	11	98	1.5×10^{-13}	1.4×10^{31}
DS Tuc A	64	160	4.9×10^3	64	36	67	12	9	5	76	63	98	4.4×10^{-13}	1.2×10^{32}
HD 63433 (2023)	24	54	0.7×10^3	46	54	30	25	15	10	66	38	90	1.1×10^{-13}	4.9×10^{30}
HD 63433 (2024)	30	71	1.1×10^3	47	53	7	23	20	36	51	7	91	1.4×10^{-13}	4.5×10^{30}

Notes. The following quantities are listed: star name, mean unsigned large-scale magnetic strength, maximum unsigned large-scale magnetic strength, total reconstructed magnetic energy, poloidal and toroidal magnetic energies as a fraction of the total energy, dipolar, quadrupolar, and octupolar magnetic energy as a fraction of the poloidal energy, axisymmetric magnetic energy as a fraction of the total energy, poloidal axisymmetric energy as a fraction of the poloidal energy, toroidal axisymmetric energy as a fraction of the toroidal energy, mass loss rate, and angular momentum loss rate. The first row of HD 63433 refers to the 2023 ZDI reconstruction (Bellotti et al. 2024) while the second row to the 2024 reconstruction presented here.

mised Voigt kernel parameters are $d = 1.95$, $w_G = 1.12 \text{ km s}^{-1}$, and $w_L = 3.0 \text{ km s}^{-1}$ and the assumed inclination is 80° . Our ten Neo-Narval observations span 23 d (or 5.2 rotational cycles), so a surface shear would have had the time to distort the LSD profiles sufficiently to be detected. The result of the differential rotation search is shown in Fig. 1. The analysis yielded $P_{\text{rot}} = 4.315 \pm 0.035 \text{ d}$ and $d\Omega = 0.189 \pm 0.089 \text{ rad d}^{-1}$, which implies a rotation period at the pole of $P_{\text{rot}} = 4.959 \pm 0.351 \text{ d}$ (see Eq. 2) and an equator-pole lap time of 33 d. The value of $d\Omega$ is consistent with typical latitudinal differential rotation rates of young solar-like stars (see Bellotti et al. 2025b, for a recent example). Although the χ_r^2 landscape features a minimum, the lower boundary of the grid features a decrease in χ_r^2 making the overall landscape shape irregular. This is reflected in a large error bar of the differential rotation rate. Moreover, Petit et al. (2002) showed that when estimating $d\Omega$ with fewer phases than about 15, rotational phase gaps tend to generate biases that are not included in the statistical error bar.

The model Stokes V profiles were fit down to $\chi_r^2 = 0.98$ (see Fig. A.1), from an initial value of 2.05 which corresponds to a featureless magnetic map. The target χ_r^2 is determined by running ZDI over a grid of χ_r^2 values with all other parameters fixed, each time recording the entropy at convergence, and by measuring the maximum of the change rate in the entropy (see Alvarado-Gómez et al. 2015, for more details).

The ZDI magnetic map is illustrated in Fig. 2 and its properties are listed in Table 3. The unsigned, mean magnetic field strength is $B_{\text{mean}} = 37 \text{ G}$, and the topology is predominantly toroidal, as the corresponding component accounts for 72% of the total magnetic energy. Of the poloidal component, the dipolar, quadrupolar, and octupolar modes store 28%, 13%, and 26% of the energy. The large-scale toroidal component is mostly axisymmetric (98%) while the poloidal component is non-axisymmetric (11%).

4.2. DS Tuc A

For DS Tuc A, the optimal Voigt kernel parameters are: $d = 0.52$, $w_G = 1.75 \text{ km s}^{-1}$, and $w_L = 4.0 \text{ km s}^{-1}$. We set the rotation period to 2.85 d, the $v_{\text{eq}} \sin(i)$ to 17.8 km s^{-1} (Newton et al. 2019), and the inclination to 80° . The search for latitudinal differential rotation was inconclusive in this case, so we assumed solid body rotation.

The model Stokes V profiles were fit down to $\chi_r^2 = 1.6$ (see Fig. A.1), from an initial value of 7.2. The target χ_r^2 of 1.6 is most likely due to unconstrained differential rotation and slightly underestimated error bars, as the actual noise in the pro-

file looks larger than the uncertainties in some instances. The ZDI magnetic map is illustrated in Fig. 2 and its properties are listed in Table 3. The unsigned, mean magnetic field strength is $B_{\text{mean}} = 64 \text{ G}$, and the topology is predominantly poloidal (64%), with the dipolar, quadrupolar, and octupolar modes accounting for 67%, 12%, and 9% of the energy. The large-scale topology is also mostly axisymmetric, with 66% of the energy in the corresponding modes.

4.3. HD 63433

For HD 63433, the optimised Voigt kernel parameters are: $d = 1.8$, $w_G = 1.1 \text{ km s}^{-1}$, and $w_L = 2.6 \text{ km s}^{-1}$. The stellar inclination was fixed to 70° and the rotational velocity to 7.3 km s^{-1} (similar to Bellotti et al. 2024). Our nine Neo-Narval observations in 2024 span 28 d (or 4.3 rotational cycles), and the differential rotation search yielded a minimum at $P_{\text{rot}} = 6.489 \pm 0.075 \text{ d}$ and $d\Omega = 0.147 \pm 0.023 \text{ rad d}^{-1}$. In a similar manner to the $d\Omega$ result of TOI-1860, the gap in the rotational phases may be introducing biases. The latitudinal differential rotation translates into a rotation period at the pole of $7.650 \pm 0.238 \text{ d}$ and an equator-pole lap time of 43 d. The range of P_{rot} values is thus compatible with the rotation period of $6.45 \pm 0.05 \text{ d}$ given by Mann et al. (2020).

The model Stokes V profiles were fit down to $\chi_r^2 = 0.85$ (see Fig. A.1), from an initial value of 5.45. The ZDI magnetic map is illustrated in Fig. 2 and its properties are listed in Table 3. The mean, unsigned magnetic field strength is $B_{\text{mean}} = 30 \text{ G}$, and the topology features 47% of the total energy in the poloidal component and 53% in the toroidal component. The poloidal component shows complexity, with the dipolar, quadrupolar, and octupolar modes storing 7%, 23%, and 20% of the magnetic energy. The large-scale toroidal component is mostly axisymmetric (90%) while the poloidal component is non-axisymmetric (7%).

This is the second ZDI reconstruction for HD 63433 after (Bellotti et al. 2024). We can compare our results with the 2023 ZDI reconstruction considering that the cadence and S/N of the observations are similar. We note a difference in the complexity of the large-scale configuration, as shown in Fig. 2 (and reported Table 3). In 2024 the magnetic field is more complex, since it has less energy in the dipolar mode and more in the octupolar and $\ell = 4$ modes.

5. Stellar wind

We simulated the stellar wind of TOI-1860, DS Tuc A, and HD 63433 using the Space Weather Modelling Framework

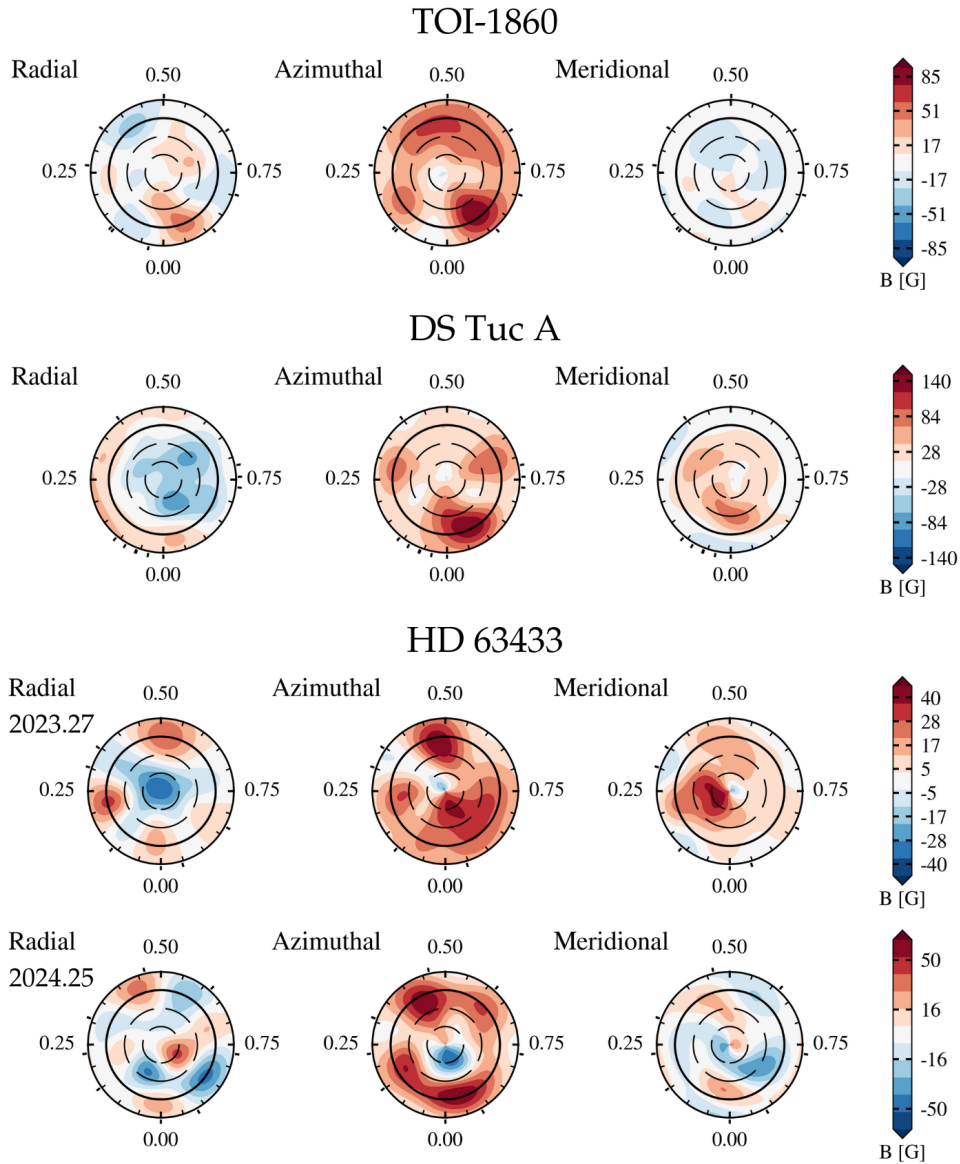


Fig. 2. Reconstructed large-scale magnetic field maps of TOI-1860, DS Tuc A, and HD 63433 in flattened polar view. For completeness, we included our previous HD 63433 reconstruction using 2023 data (Bellotti et al. 2024). From the left, the radial, azimuthal, and meridional components of the magnetic field vector are illustrated. Concentric circles represent different stellar latitudes: -30° , $+30^\circ$, and $+60^\circ$ (dashed lines), as well as the equator (solid line). The radial ticks are located at the rotational phases when the observations were collected. The rotational phases are computed with Eq. 3. The colour bar indicates the polarity and strength (in G) of the magnetic field.

(SWMF, Tóth et al. 2005, 2012) and specifically the Alfvén wave solar model (AWSOM, Sokolov et al. 2013; van der Holst et al. 2014) applied to the ZDI reconstructions described in Sect 4. A detailed description of the methodology behind the wind models can be found in the recent works of Ó Fionnagáin et al. (2019), Kavanagh et al. (2019), Evensberger et al. (2021), Alvarado-Gómez et al. (2022), Evensberger et al. (2022), Boro Saikia et al. (2023) and Evensberger et al. (2023). Here, we briefly summarise the main features of the model. The three-dimensional simulations of the stellar wind are performed by numerically solving the ideal two-temperature magnetohydrodynamic equations, letting the models converge towards a steady state solution in which balance between the magnetic and hydrodynamic forces is reached across the domain of the simulation (a summary of the equations is given in Evensberger et al. 2021).

Our AWSOM model extends from the chromosphere (that is, the inner boundary), where the temperature is set at 5×10^4 K and the number density is set at $2 \times 10^{11} \text{ m}^{-3}$, through the transition region to the stellar corona. In the AWSOM model, the stellar corona is heated by dissipation of Alfvén waves emanating from deeper stellar layers, resulting in a Poynting flux Π_A proportional to the local $|\mathbf{B}|$ value at the inner model boundary. Boro Saikia et al. (2023) used FUV emission lines forming in the chromosphere and the transition region to measure the velocity associated to the non-thermal processes that drive the solar and stellar wind. They found that the non-thermal velocities of Sun-like stars can have similar values as that observed in the solar chromosphere and transition region, hence we expect the energy density of Alfvén waves to resemble that of the Sun. The propagation and partial reflection of the Alfvén waves results in a turbulent cascade that heats and accelerates the solar wind (van

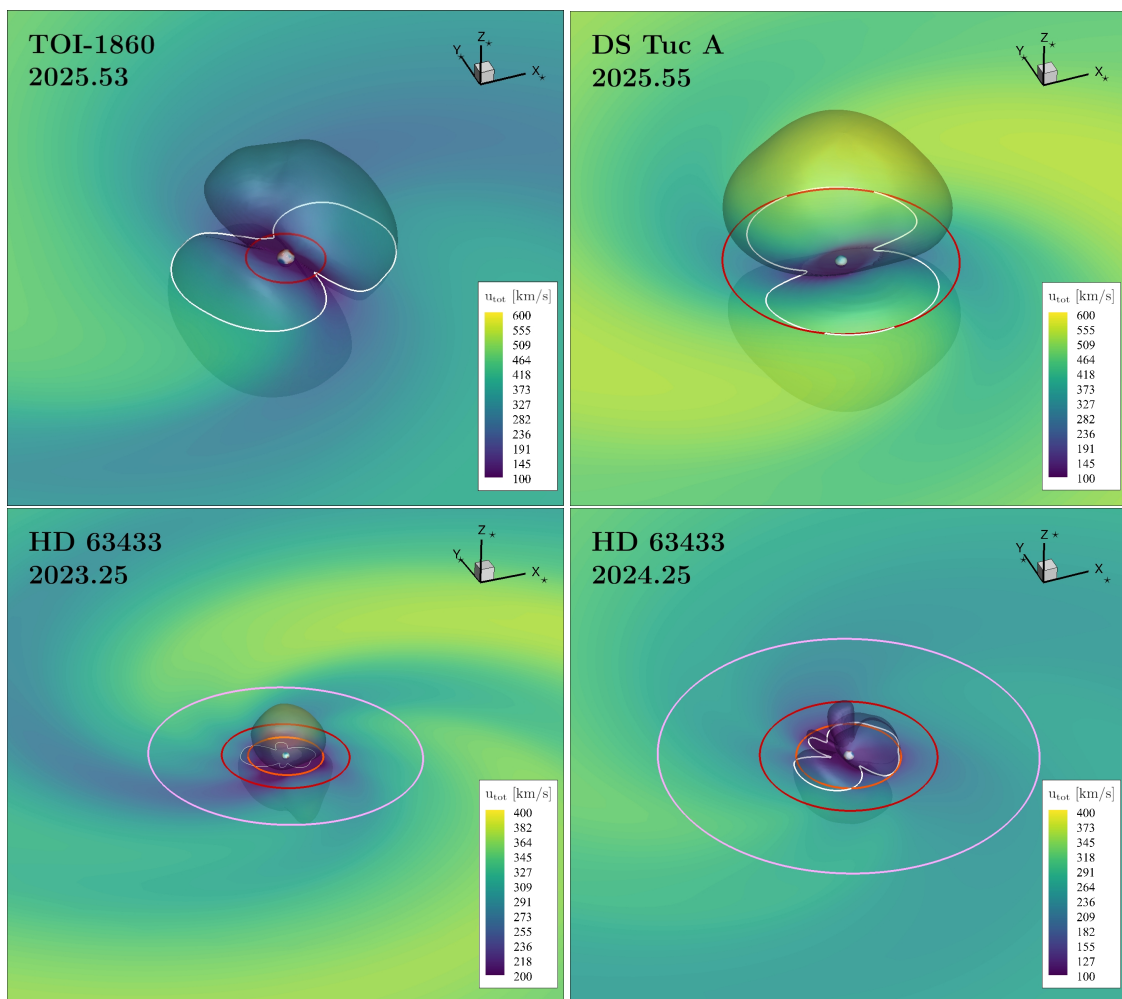


Fig. 3. Simulated stellar wind of TOI-1860, DS Tuc A, and HD 63433 in the $x_* - y_*$ plane. The rotation axis lies along the positive z_* . The Alfvén surface is shown as a translucent surface and its intersection on the $x_* - y_*$ plane is shown as a white curve. The colour bar indicates the total wind velocity. The orbits of the hosted exoplanets are also included as coloured ellipses. For HD 63433, we also show the simulations from the 2023 data analysed in Bellotti et al. (2024).

der Holst et al. 2014; Gombosi et al. 2018). We set the Poynting flux-to-field ratio to $1.1 \times 10^5 \text{ erg cm}^{-2} \text{ G}^{-1}$, the same one as used in solar wind models, and the turbulence correlation length to $1.5 \times 10^9 \text{ m T}^{1/2}$.

The models fix the large-scale radial field component at the inner boundary to the ZDI-derived values (see Fig. 2), while the transverse components are left to evolve as the numerical solution relaxes towards steady state. We emphasise that, except for the stellar mass, radius, rotation period and large-scale magnetic field, the input parameters of the AWSOM model were set to solar values that have been shown to reproduce solar wind conditions (Meng et al. 2015; van der Holst et al. 2019; Sachdeva et al. 2019).

5.1. Characteristics of the wind

The results of our three-dimensional simulations for TOI-1860, DS Tuc A, and HD 63433 are presented in Fig. 3. We also include the simulation of HD 63433 obtained from 2023 data and presented in Bellotti et al. (2024). Each panel is centred on the star and shows the steady-state solution of the stellar wind, colour-coded by the total wind speed $u_{\text{tot}} = \sqrt{u_x^2 + u_y^2 + u_z^2}$. Moving away from the star, the wind exhibits a spiral shape owing

to stellar rotation, and the wind speed (\mathbf{u}) increases while the local wind density (ρ_w) and magnetic field (B_w) decrease, as expected. The panels also illustrate the Alfvén surface, which is the boundary where the local wind speed matches the Alfvén wave velocity. The latter represents the velocity of magnetic waves propagating through plasma and it is expressed in cgs units as $v_A = B_w / \sqrt{4\pi\rho_w}$. As we subsequently discuss in Sect. 5.2, the Alfvén surface is a key factor to determine the possibility of magnetic star-planet interactions (e.g. Vidotto 2025).

For most of our stars, the Alfvén surface appears predominantly two-lobed, as expected for stars with dominant dipolar large-scale field configurations (e.g. Evensberget et al. 2023). Consistently with the ZDI reconstructions described in Sect. 4, the Alfvén surface of HD 63433 features a larger and more complex shape than TOI-1860 and DS Tuc A, and than our previous wind simulation of HD 63433 corresponding to 2023 data (see Bellotti et al. 2024). This temporal evolution of the Alfvén surface, which correlates with the evolution of the large-scale magnetic field, can modulate magnetic star-planet interactions.

We computed the mass loss rate (\dot{M}) by integrating the mass flux over a closed spherical surface (Σ) centred on the star

$$\dot{M} = \oint_{\Sigma} \rho \mathbf{u} \cdot \hat{\mathbf{n}} d\Sigma, \quad (4)$$

where ρ and \mathbf{u} are the stellar wind density and speed of our steady-state solution. As listed in Table 3, we estimated values between 5 and 20 times larger than the solar wind-mass loss rate. We note that \dot{M} should not vary with the choice of surface Σ , as long as such surface encloses the star and the model has reached steady state. We found variations for less than 1% by changing the spherical surface radius across the simulation domain, as a numerical check to ensure that the simulation has reached steady-state. The values of \dot{M} are reported in Table 3.

We then computed the angular momentum loss rate (\dot{J}), which regulates the spin-down of the star with age. Following Mestel (1999) and Vidotto et al. (2014),

$$\dot{J} = \oint_{\Sigma} \left[-\frac{\varpi B_{\varphi} B_r}{4\pi} + \varpi \rho u_{\varphi} u_r \right] d\Sigma, \quad (5)$$

where $\varpi = \sqrt{(x^2 + y^2)}$ is the cylindrical radius and (B_r, u_r) and $(B_{\varphi}, u_{\varphi})$ are the radial and azimuthal components of the magnetic field and speed of the stellar wind. We estimated values between a factor of 1.4 and 35 larger than the average angular momentum loss rate of the Sun computed for cycle 23-24 (Finley et al. 2019), and all conserved at most within 5%. The values of \dot{J} are reported in Table 3.

5.2. Environment at the planetary orbit

We now describe the stellar wind characteristics at the orbits of the known exoplanets, which are illustrated in Fig. 3 as coloured ellipses around the stars. Quantitative information of the wind conditions at these orbits and the location relative to the Alfvén surface are shown in Fig. 4. Using the planetary frame as a reference, we computed the variations of wind density, relative speed ($\Delta\mathbf{u}$), ram pressure and Alfvén Mach number during one stellar rotation. The relative speed is between the wind velocity and the Keplerian velocity of the planet $\Delta\mathbf{u} = \mathbf{u} - \mathbf{v}_K$, and it is used to compute the ram pressure experienced by the planet $P_{\text{ram}} = \rho_w \Delta u^2$. The Alfvén Mach number is the ratio between the Alfvén wave velocity and the wind speed, $M_A = \Delta u/v_A$, and it is a practical quantity to determine whether an orbit is in sub-Alfvénic regime $M_A < 1$ or in super-Alfvénic regime $M_A > 1$.

TOI-1860 is a young (133 Myr) K1-type star hosting one known planet at 0.02 au or 1.066 d orbit as revealed by *TESS* observations (Giacalone et al. 2022). The planet radius is $1.31 R_{\oplus}$, the equilibrium temperature is 1885 K and the authors estimated a mass of $2.2 M_{\oplus}$ from the probabilistic relation of Chen & Kipping (2017). The eccentricity of the planetary orbit has not been constrained yet in the literature, hence we assumed a circular orbit in the equatorial plane of the star with radius equal to $4.66 R_{\star}$ (with $R_{\star} = 0.94 R_{\odot}$). As shown in the first column of Fig. 4, the average wind density and speed are $7.9 \times 10^{-19} \text{ g/cm}^3$ and 260 km/s, and the planet experiences an average ram pressure of $4.2 \times 10^{-4} \text{ dyn/cm}^2$. The two dips (or peaks) stem from the spiral morphology of the wind, which is in turn shaped by the change of polarity of the dipolar component. The orbit of TOI-1860 b is predominantly sub-Alfvénic and becomes super-Alfvénic briefly between phases 0.23-0.29 and 0.81-0.82.

DS Tuc A is a young (45 Myr) G5-type star in a visual binary system together with the K3-type star DS Tuc B at a separation of 5 arcsec (Torres et al. 2006). The primary component hosts a $5.7 R_{\oplus}$, super-Neptune planet at an orbital distance of 0.18 au or period of 8.1 d (Newton et al. 2019; Benatti et al. 2019). By modelling radial velocity observations, Benatti et al. (2019) estimated an upper limit on the exoplanet's mass of $1.3 M_{\text{Nep}}$ and

they considered the planet to be potentially inflated. Recent simulations by King et al. (2025) of future scenarios for the exoplanet showed that, at 5 Gyr, it may become a Neptune-sized planet or a super-Earth stripped of its primordial H/He envelope. Assuming a circular orbit in the equatorial plane of the star at $20.35 R_{\star}$ (Newton et al. 2019) where $R_{\star} = 0.96 R_{\odot}$, we found an average wind density, speed, and ram pressure of $4.2 \times 10^{-20} \text{ g/cm}^3$, 430 km/s, and $6.5 \times 10^{-5} \text{ dyn/cm}^2$. We note that these values vary of less than 10% if we assume the orbital distance of $19.42 R_{\star}$ obtained by Benatti et al. (2019). We found that the orbit of the planet is trans-Alfvénic, since parts of it are sub-Alfvénic (orbital phases between 0.07-0.31 and 0.58-0.83) while the rest is super-Alfvénic.

HD 63433 is a young (414 Myr) G5-type star hosting three planets at 0.05 au (planet d), 0.07 au (planet b), 0.14 au (planet c Capistrant et al. 2024). The orbital periods are 4.2 d, 7.11 d, and 20.55 d, and the radii are $1.07 R_{\oplus}$, $2.02 R_{\oplus}$, and $2.44 R_{\oplus}$ (see also Mann et al. 2020; Mallorquín et al. 2023; Damasso et al. 2023). From radial velocity observations, Damasso et al. (2023) measured planetary mass upper limits of $11 M_{\oplus}$ for planet b and $31 M_{\oplus}$ for planet c, while Mallorquín et al. (2023) measured $22 M_{\oplus}$ for planet b and $15.5 M_{\oplus}$ for planet c.

Following Bellotti et al. (2024), we assumed that the planets have circular orbits in the equatorial plane of the star with radii of $16.8 R_{\star}$, $36.1 R_{\star}$, and $9.9 R_{\star}$ for planet b, c, and d (with $R_{\star} = 0.897 R_{\odot}$). For planet b, the average wind density, speed, and ram pressure are $2.9 \times 10^{-20} \text{ g/cm}^3$, 250 km/s, and $1.7 \times 10^{-5} \text{ dyn/cm}^2$. For planet c, these values are $5.3 \times 10^{-21} \text{ g/cm}^3$, 275 km/s, and $3.9 \times 10^{-6} \text{ dyn/cm}^2$. For planet d, these values are $1.2 \times 10^{-19} \text{ g/cm}^3$, 214 km/s, and $5.1 \times 10^{-5} \text{ dyn/cm}^2$.

As for the 2023 observations, the orbits of planet b and c are super-Alfvénic (see Bellotti et al. 2024). For planet d, the Alfvén surface encompasses a larger fraction of the planetary orbit compared to the simulation of 2023 wind conditions (see Fig. 4), owing to the temporal evolution and intensification of the large-scale magnetic field. More specifically, the orbit of planet d was sub-Alfvénic between phases 0.38-0.50, while in our new simulation it is between phases 0.00-0.20, 0.45-0.69, and 0.86-1.00 (see the lower right panel of Fig. 4).

6. Conclusions

With this work, we follow Bellotti et al. (2024) and provide an update on the results of the spectropolarimetric campaign dedicated to characterise the magnetic field of known exoplanet host stars belonging to the current *Ariel* candidate sample. Our programme aims to collect information on the magnetic activity of a representative sample to inform the observing strategy of *Ariel*. We analysed spectropolarimetric observations of 15 stars obtained with Neo-Narval, HARPSpol, and SPIRou.

We did not detect circularly polarised Zeeman signatures in eight stars over multiple snapshot observations. We detected Zeeman signatures for TOI-1136, TOI-1860, DS Tuc A, and the newest observations of HD 63433, and we obtained one marginal detection for TOI-836 and two for TOI-2076. We estimated absolute longitudinal magnetic field values of the order of 5 to 50 G for these stars, which is in agreement with previous studies of fast-rotating, solar-like stars (e.g. Petit et al. 2005, 2008; Marsden et al. 2014; Folsom et al. 2016; Brown et al. 2022).

We performed the reconstruction of the large-scale magnetic field via ZDI for TOI-1860, DS Tuc A, and HD 63433, but not TOI-1136, since we did not have a sufficient number of observations. For TOI-1860 and DS Tuc A, this is the first reconstruction of the large-scale magnetic field. For TOI-1860, we

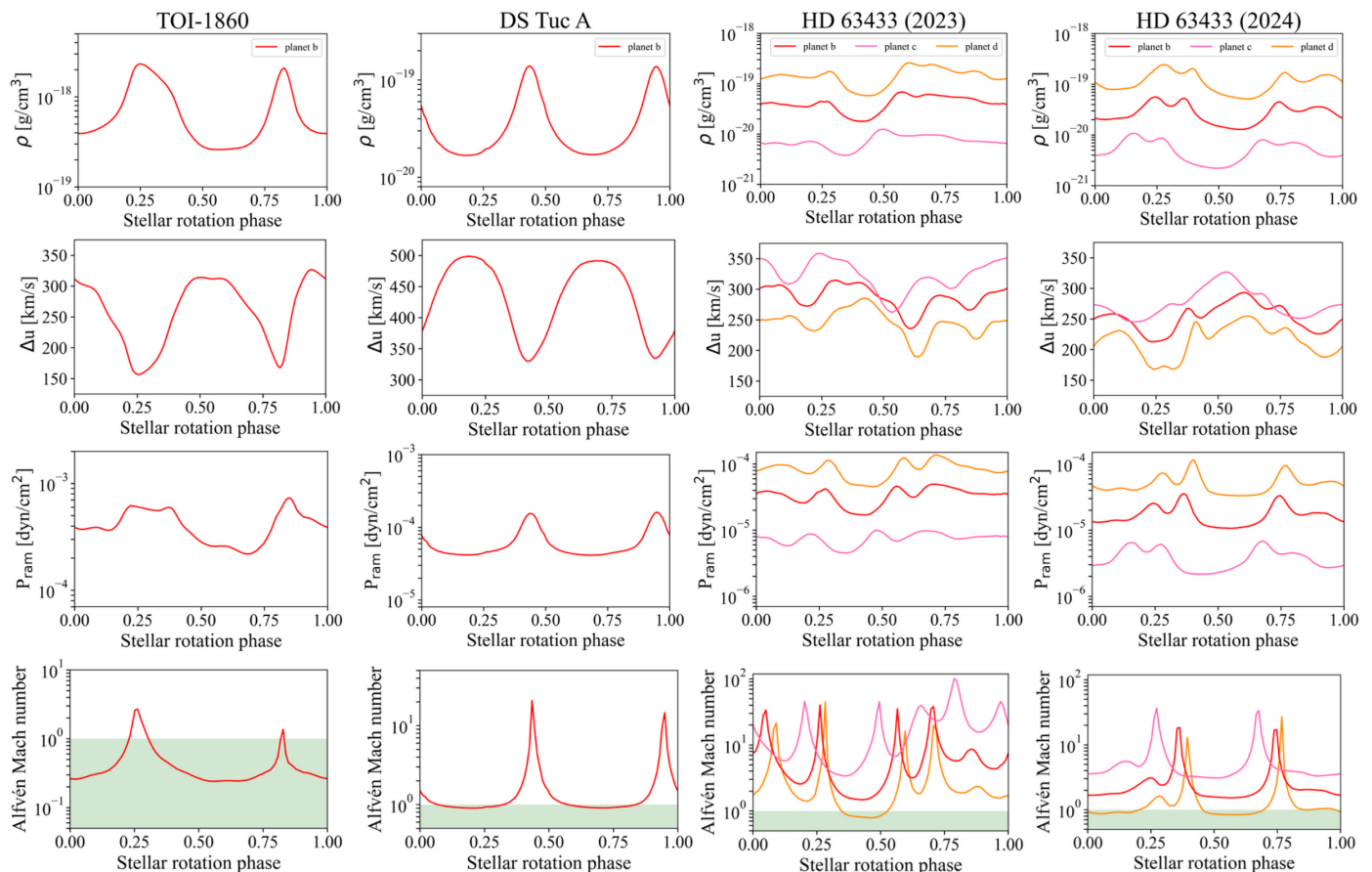


Fig. 4. Stellar wind conditions in the planetary frame as a function of stellar rotation phase. From the left, the columns refer to the TOI-1860, DS Tuc A, HD 63433 (2023), and HD 63433 (2024) systems. From the top, the panels show the wind density (ρ), relative velocity (Δu), ram pressure (P_{ram}), and Alfvén Mach number (M_A). The sub-Alfvénic regime ($M_A < 1$) of the stellar wind is shown as a green shaded region. In the M_A panel of HD 63433, we also show the computation for planet d from 2023 data as a dashed line (see Bellotti et al. 2024).

found a predominantly toroidal and moderately axisymmetric large-scale magnetic field with an average strength of 37 G. For DS Tuc A, we found a poloidal magnetic field that is mostly dipolar and axisymmetric with an average field strength of 64 G. For HD 63433, our new 2024 observations revealed a more complex topology compared to the 2023 map, with more energy stored in the $\ell = 3$ and $\ell = 4$ modes at the expenses of the $\ell = 1$ mode. The other features are similar: $\sim 50\%$ poloidal, moderately axisymmetric and with an average field strength of 70 G. In a broader context, the ZDI reconstructions of these stars are in agreement with the large-scale field configuration of young, solar-like stars which are known to exhibit variability also of the order of one year (see Folsom et al. 2016; Willamo et al. 2022; Bellotti et al. 2025a, for recent examples).

Finally, we used the magnetic field reconstructions to numerically model the stellar wind environment and compute the location of the Alfvén surface. As expected for dipole-dominated, large-scale magnetic field topologies, the shape of the Alfvén surface is predominantly two-lobed. For HD 63433, the complexity of the large-scale field, that is the deviation from being simply dipolar, translates in a more complex configuration of the Alfvén surface as well. Based on the location of the Alfvén surface, we then evaluated the regime in which the hosted exoplanets are orbiting (see Vidotto 2025, for a recent review).

We found that the orbit of TOI-1860 b is almost completely sub-Alfvénic, meaning that a direct connection between the planet and the stellar magnetic field can occur. As a result, the

orbital motion of the planet can generate Alfvén waves propagating towards the star or magnetic reconnection events (e.g. Neubauer 1998; Ip et al. 2004; Saur et al. 2013; Strugarek et al. 2015; Kavanagh et al. 2022). From the recent work of Presa et al. (2024), assuming the planetary magnetic field to be dipolar and with a certain obliquity, we expect the planetary atmospheric escape in sub-Alfvénic regime to occur via a single polar outflow, which was found to be weaker than the bipolar outflow typical of super-Alfvénic interactions (Carolan et al. 2021a). We also note that, given the young age of the system, XUV irradiation would also be an important source of atmospheric mass loss.

There are several ways with which the stellar wind can affect atmospheric escape in exoplanets. They can reduce escape rates (Vidotto & Cleary 2020), change signatures of atmospheric evaporation through spectroscopic transits (Carolan et al. 2021b), and possibly generate a tenuous atmosphere through sputtering processes (Vidotto et al. 2018). With the constrained stellar wind properties presented in our work, future atmospheric models of exoplanets will be able to better pin-point the effects of the wind of the host star on the planet’s upper atmosphere, as well as potential signatures in Ly- α and He I transits. For Ariel specifically, such models are important to assess the presence and evolution of an exoplanet atmosphere (Kubyskhina et al. 2022), as well as to interpret the planetary atmospheric response to stellar activity (e.g. upper-atmosphere heating, ionisation, and chemistry García Muñoz 2023; Strugarek et al. 2025).

The orbits of HD 63433 b and c are super-Alfvénic, in a similar manner as the previous stellar wind model from 2023 data (see Bellotti et al. 2024). In this regime, which is reminiscent of the regime in which Solar System planets orbit, we expect the formation of a bow shock between a potential planetary magnetosphere and the stellar wind (Chapman & Ferraro 1931; Vidotto et al. 2009, 2010), as well as the presence of evaporated planetary material in the shape of a tail (e.g. Schneider et al. 2007; Villarreal D’Angelo et al. 2018). Finally, planets DS Tuc A b and HD 63433 d are in the trans-Alfvénic region, where the stellar wind conditions can alternate between super- and sub-Alfvénic. For HD 63433 d, we note that sub-Alfvénic fraction of the orbit is increased relative to the model from 2023 data, owing to the temporal variability of the stellar large-scale magnetic field. Finally, we also note that the Alfvén surface in our model is mostly dictated by the ratio between the Poynting flux and the magnetic field strength reconstructed with ZDI. Such reconstructions may lead to an underestimated magnetic field strength (Lehmann et al. 2019), ultimately affecting the size of the Alfvén surface (see e.g. Fig. 5 Kavanagh et al. 2021).

At this point, additional observations are required to confirm whether the large-scale magnetic field is detectable for certain exoplanet host stars. An example of uncertain magnetic field detection is TOI-2076, for which we found two marginal detections and four non-detections, while Damasso et al. (2024) corroborated its magnetic activity and a long-term variation of ~ 2.7 yr. Furthermore, our results motivate the spectropolarimetric monitoring of the presented sub-sample of potential *Ariel* stars on the long-term. Such a monitoring can address the question of whether the stars manifest magnetic cycles and if so, how they relate to the activity cycles discovered with other techniques. For instance, DS Tuc A exhibits a long-term photometric variation of ~ 8 yr, as described by Benatti et al. (2019). Ultimately, this will be valuable to constrain the temporal evolution of the Alfvén surface and of the observational signatures marking magnetic star-planet interactions, as well as the evolution of evaporating atmospheres and their interactions with the stellar wind.

The spectropolarimetric programme presented here started in 2022 and it is expected to continue until the launch of *Ariel*, with the aim of informing observing strategies for specific targets as well as atmospheric modelling. Once the mission is launched, the goal of the campaign will become of a follow-up nature, thus complementing the observations already performed and providing new insights for the interpretation of *Ariel* data. The *Ariel* Candidate Sample is subject to yearly adjustments based on new analyses of the most suitable targets for atmospheric characterisation, but also in light of new exoplanet discoveries. Although it is hard to estimate a number of targets given the dynamic nature of the Candidate Sample combined with our selection criteria for magnetically active stars, we expect between two and five additional stars per year, for which to assess the magnetic field detectability and reconstruct the topology.

7. Data Availability

The spectropolarimetric observations analysed in this work are available on online databases. All Neo-Narval and SPIRou observations are available on PolarBase⁸ (Petit et al. 2014). The Neo-Narval observations were taken under the programmes L232N02, L241N09, and L251N08 and the SPIRou observations under the programmes 22BF97, 23AF16, 23BF98, and 24AF99. The HARPSPol observations are available at the ESO Science

Archive⁹ under the programmes 110.24C8.001, 110.24C8.002, 115.28DD.001, and 115.28DD.002.

Acknowledgements. This publication is part of the project “Exo-space weather and contemporaneous signatures of star-planet interactions” (with project number OCENW.M.22.215 of the research programme “Open Competition Domain Science- M”), which is financed by the Dutch Research Council (NWO). This work used the Dutch national e-infrastructure with the support of the SURF Cooperative using grant nos. EINF-2218 and EINF-5173. This work has been developed within the framework of the Ariel “Stellar Characterisation” and “Stellar Activity” working groups, in synergy with the “Planetary Formation” working group of the ESA *Ariel* space mission Consortium. AAV and DE acknowledge funding from the European Research Council (ERC) under the European Union’s Horizon 2020 research and innovation programme (grant agreement No 817540, ASTROFLOW). AAV acknowledges funding from the Dutch Research Council (NWO), with project number VI.C.232.041 of the Talent Programme Vici. We thank the TBL team for providing service observing with Neo-Narval under the programmes L232N02, L241N09, and L251N08 (PI S. Bellotti). Based on observations obtained at the Canada-France-Hawaii Telescope (CFHT) which is operated by the National Research Council of Canada, the Institut National des Sciences de l’Univers of the Centre National de la Recherche Scientifique of France, and the University of Hawaii. The observations were collected under the programmes 22BF97, 23AF16, 23BF98, and 24AF99 (PI S. Bellotti and P. Petit). Based on observations collected at the European Southern Observatory under ESO programmes 110.24C8.001, 110.24C8.002, 115.28DD.001, and 115.28DD.002 (PI. S. Bellotti). This research has made use of the NASA Exoplanet Archive, which is operated by the California Institute of Technology, under contract with the National Aeronautics and Space Administration under the Exoplanet Exploration Program. This work made use of the Ariel Stellar Catalogue developed by the Stellar Characterisation WG in preparation of the ESA *Ariel* space mission. This work used the BATS-R-US tools developed at the University of Michigan Center for Space Environment Modeling and made available through the NASA Community Coordinated Modeling Center. This work has made use of the VALD database, operated at Uppsala University, the Institute of Astronomy RAS in Moscow, and the University of Vienna; Astropy, 12 a community-developed core Python package for Astronomy (Astropy Collaboration et al. 2013, 2018); NumPy (van der Walt et al. 2011); Matplotlib: Visualization with Python (Hunter 2007); SciPy (Virtanen et al. 2020) and PyAstronomy (Czesla et al. 2019).

References

- Alvarado-Gómez, J. D., Cohen, O., Drake, J. J., et al. 2022, *ApJ*, 928, 147
 Alvarado-Gómez, J. D., Hussain, G. A. J., Grunhut, J., et al. 2015, *A&A*, 582, A38
 Angus, R., Morton, T., Aigrain, S., Foreman-Mackey, D., & Rajpaul, V. 2018, *MNRAS*, 474, 2094
 Astropy Collaboration, Price-Whelan, A. M., Sipőcz, B. M., et al. 2018, *AJ*, 156, 123
 Astropy Collaboration, Robitaille, T. P., Tollerud, E. J., et al. 2013, *A&A*, 558, A33
 Bagnulo, S., Landolfi, M., Landstreet, J. D., et al. 2009, *PASP*, 121, 993
 Bellotti, S., Evensberger, D., Vidotto, A. A., et al. 2024, *A&A*, 688, A63
 Bellotti, S., Fares, R., Vidotto, A. A., et al. 2023a, *A&A*, 676, A139
 Bellotti, S., Lüftinger, T., Boro Saikia, S., et al. 2025a, *A&A*, 700, A282
 Bellotti, S., Morin, J., Lehmann, L. T., et al. 2023b, *A&A*, 676, A56
 Bellotti, S., Petit, P., Jeffers, S. V., et al. 2025b, *A&A*, 693, A269
 Benatti, S., Nardiello, D., Malavolta, L., et al. 2019, *A&A*, 630, A81
 Boro Saikia, S., Lueftinger, T., Airapetian, V. S., et al. 2023, *ApJ*, 950, 124
 Boro Saikia, S., Lueftinger, T., Jeffers, S. V., et al. 2018, *A&A*, 620, L11
 Brown, E. L., Jeffers, S. V., Marsden, S. C., et al. 2022, *MNRAS*, 514, 4300
 Canto Martins, B. L., Gomes, R. L., Messias, Y. S., et al. 2020, *ApJS*, 250, 20
 Capistrant, B. K., Soares-Furtado, M., Vanderburg, A., et al. 2024, *AJ*, 167, 54
 Carolan, S., Vidotto, A. A., Hazra, G., Villarreal D’Angelo, C., & Kubyskhina, D. 2021a, *MNRAS*, 508, 6001
 Carolan, S., Vidotto, A. A., Villarreal D’Angelo, C., & Hazra, G. 2021b, *MNRAS*, 500, 3382
 Chageat, Q., Keyte, L., Waldmann, I. P., & Tinetti, G. 2020, *ApJ*, 896, 107
 Chapman, S. & Ferraro, V. C. A. 1931, *Terrestrial Magnetism and Atmospheric Electricity (Journal of Geophysical Research)*, 36, 77
 Chen, J. & Kipping, D. 2017, *ApJ*, 834, 17
 Claret, A. & Bloemen, S. 2011, *A&A*, 529, A75
 Cook, N. J., Artigau, É., Doyon, R., et al. 2022, *PASP*, 134, 114509
 Cotton, D. V., Evensberger, D., Marsden, S. C., et al. 2019, *MNRAS*, 483, 1574

⁸ <https://www.polarbase.ovgso.fr/>

⁹ See <https://archive.eso.org/wdb/wdb/eso/repro/form>

- Czesla, S., Schröter, S., Schneider, C. P., et al. 2019, *PyA: Python astronomy-related packages*
- Dai, F., Masuda, K., Beard, C., et al. 2023, *AJ*, 165, 33
- Damasso, M., Locci, D., Benatti, S., et al. 2024, *A&A*, 690, A235
- Damasso, M., Locci, D., Benatti, S., et al. 2023, *A&A*, 672, A126
- Danielski, C., Brucalassi, A., Benatti, S., et al. 2022, *Experimental Astronomy*, 53, 473
- Di Maio, C., Changeat, Q., Benatti, S., & Micela, G. 2023, *A&A*, 669, A150
- Donati, J. F. 2003, in *Astronomical Society of the Pacific Conference Series*, Vol. 307, *Solar Polarization*, ed. J. Trujillo-Bueno & J. Sanchez Almeida, 41
- Donati, J. F. & Brown, S. F. 1997, *A&A*, 326, 1135
- Donati, J.-F., Cristofari, P. I., Finociety, B., et al. 2023, *MNRAS*, 525, 455
- Donati, J.-F., Forveille, T., Collier Cameron, A., et al. 2006, *Science*, 311, 633
- Donati, J. F., Kouach, D., Moutou, C., et al. 2020, *MNRAS*, 498, 5684
- Donati, J. F., Mengel, M., Carter, B. D., et al. 2000, *MNRAS*, 316, 699
- Donati, J. F., Semel, M., Carter, B. D., Rees, D. E., & Collier Cameron, A. 1997, *MNRAS*, 291, 658
- Edwards, B., Mugnai, L., Tinetti, G., Pascale, E., & Sarkar, S. 2019, *AJ*, 157, 242
- Edwards, B. & Tinetti, G. 2022, *AJ*, 164, 15
- Evensberget, D., Carter, B. D., Marsden, S. C., Brookshaw, L., & Folsom, C. P. 2021, *MNRAS*, 506, 2309
- Evensberget, D., Carter, B. D., Marsden, S. C., et al. 2022, *MNRAS*, 510, 5226
- Evensberget, D., Marsden, S. C., Carter, B. D., et al. 2023, *MNRAS*, 524, 2042
- Finley, A. J., Hewitt, A. L., Matt, S. P., et al. 2019, *ApJ*, 885, L30
- Folsom, C. P., Bouvier, J., Petit, P., et al. 2018, *MNRAS*, 474, 4956
- Folsom, C. P., Erba, C., Petit, V., et al. 2025, *Journal of Open Source Software*, 10, 7891
- Folsom, C. P., Ó Fionnagáin, D., Fossati, L., et al. 2020, *A&A*, 633, A48
- Folsom, C. P., Petit, P., Bouvier, J., et al. 2016, *MNRAS*, 457, 580
- Frazier, R. C., Stefánsson, G., Mahadevan, S., et al. 2023, *ApJ*, 944, L41
- García Muñoz, A. 2023, *A&A*, 672, A77
- Garraffo, C., Drake, J. J., & Cohen, O. 2016, *ApJ*, 833, L4
- Genest, F., Lafrenière, D., Boucher, A., et al. 2022, *AJ*, 163, 231
- Giacalone, S., Dressing, C. D., Hedges, C., et al. 2022, *AJ*, 163, 99
- Gombosi, T. I., van der Holst, B., Manchester, W. B., & Sokolov, I. V. 2018, *Living Reviews in Solar Physics*, 15, 4
- Güdel, M. 2004, *A&A Rev.*, 12, 71
- Hahlin, A., Kochukhov, O., Rains, A. D., et al. 2023, *A&A*, 675, A91
- Hara, N. C., Bouchy, F., Stalport, M., et al. 2020, *A&A*, 636, L6
- Hawthorn, F., Bayliss, D., Wilson, T. G., et al. 2023, *MNRAS*, 520, 3649
- Hazra, G., Vidotto, A. A., & D'Angelo, C. V. 2020, *MNRAS*, 496, 4017
- Hunter, J. D. 2007, *Computing in Science and Engineering*, 9, 90
- Hussain, G. A. J., Collier Cameron, A., Jardine, M. M., et al. 2009, *MNRAS*, 398, 189
- Ip, W.-H., Kopp, A., & Hu, J.-H. 2004, *ApJ*, 602, L53
- Johnstone, C. P., Bartel, M., & Güdel, M. 2021, *A&A*, 649, A96
- Kavanagh, R. D., Vidotto, A. A., Klein, B., et al. 2021, *MNRAS*, 504, 1511
- Kavanagh, R. D., Vidotto, A. A., Ó Fionnagáin, D., et al. 2019, *MNRAS*, 485, 4529
- Kavanagh, R. D., Vidotto, A. A., Vedantham, H. K., et al. 2022, *MNRAS*, 514, 675
- King, G. W., Corrales, L. R., Bourrier, V., et al. 2025, *ApJ*, 980, 27
- Klein, B., Donati, J.-F., Moutou, C., et al. 2021, *MNRAS*, 502, 188
- Kochukhov, O., Hackman, T., Lehtinen, J. J., & Wehrhahn, A. 2020, *A&A*, 635, A142
- Kochukhov, O., Makaganiuk, V., & Piskunov, N. 2010, *A&A*, 524, A5
- Kubyskhina, D., Vidotto, A. A., Villarreal D'Angelo, C., et al. 2022, *MNRAS*, 510, 2111
- Lammer, H., Selsis, F., Ribas, I., et al. 2003, *ApJ*, 598, L121
- Landi Degl'Innocenti, E. 1992, *Magnetic field measurements.*, ed. F. Sanchez, M. Collados, & M. Vazquez, 71
- Lanza, A. F. 2013, *A&A*, 557, A31
- Lehmann, L. T. & Donati, J. F. 2022, *MNRAS*, 514, 2333
- Lehmann, L. T., Donati, J. F., Fouqué, P., et al. 2024, *MNRAS*, 527, 4330
- Lehmann, L. T., Hussain, G. A. J., Jardine, M. M., Mackay, D. H., & Vidotto, A. A. 2019, *MNRAS*, 483, 5246
- Locci, D., Aresu, G., Petralia, A., et al. 2024, *The Planetary Science Journal*, 5, 58
- Locci, D., Petralia, A., Micela, G., et al. 2022, *The Planetary Science Journal*, 3, 1
- López Ariste, A., Georgiev, S., Mathias, P., et al. 2022, *A&A*, 661, A91
- Luque, R., Fulton, B. J., Kunimoto, M., et al. 2022, *A&A*, 664, A199
- Magrini, L., Danielski, C., Bossini, D., et al. 2022, *A&A*, 663, A161
- Mallorquín, M., Béjar, V. J. S., Lodieu, N., et al. 2023, *A&A*, 671, A163
- Mancini, L., Esposito, M., Covino, E., et al. 2018, *A&A*, 613, A41
- Mann, A. W., Johnson, M. C., Vanderburg, A., et al. 2020, *AJ*, 160, 179
- Marsden, S. C., Petit, P., Jeffers, S. V., et al. 2014, *MNRAS*, 444, 3517
- Mayor, M., Pepe, F., Queloz, D., et al. 2003, *The Messenger*, 114, 20
- Mazeh, T., Perets, H. B., McQuillan, A., & Goldstein, E. S. 2015, *ApJ*, 801, 3
- McCann, J., Murray-Clay, R. A., Kratter, K., & Krumholz, M. R. 2019, *ApJ*, 873, 89
- McComas, D. J. 2003, in *American Institute of Physics Conference Series*, Vol. 679, *Solar Wind Ten*, ed. M. Velli, R. Bruno, F. Malara, & B. Bucci (AIP), 33–38
- Meng, X., van der Holst, B., Tóth, G., & Gombosi, T. I. 2015, *MNRAS*, 454, 3697
- Mestel, L. 1999, *Stellar magnetism*
- Moutou, C., Donati, J. F., Savalle, R., et al. 2007, *A&A*, 473, 651
- Mugnai, L. V., Pascale, E., Edwards, B., Papageorgiou, A., & Sarkar, S. 2020, *Experimental Astronomy*, 50, 303
- Neubauer, F. M. 1998, *J. Geophys. Res.*, 103, 19843
- Newton, E. R., Mann, A. W., Tofflemire, B. M., et al. 2019, *ApJ*, 880, L17
- Nicholson, B. A., Vidotto, A. A., Mengel, M., et al. 2016, *MNRAS*, 459, 1907
- Ó Fionnagáin, D., Vidotto, A. A., Petit, P., et al. 2019, *MNRAS*, 483, 873
- Osborn, H. P., Bonfanti, A., Gandolfi, D., et al. 2022, *A&A*, 664, A156
- Oshagh, M., Santos, N. C., Boisse, I., et al. 2013, *A&A*, 556, A19
- Petit, P., Dintrans, B., Solanki, S. K., et al. 2008, *MNRAS*, 388, 80
- Petit, P., Donati, J. F., Aurière, M., et al. 2005, *MNRAS*, 361, 837
- Petit, P., Donati, J. F., & Collier Cameron, A. 2002, *MNRAS*, 334, 374
- Petit, P., Louge, T., Théado, S., et al. 2014, *PASP*, 126, 469
- Piskunov, N., Snik, F., Dolgopopov, A., et al. 2011, *The Messenger*, 143, 7
- Piskunov, N., Wehrhahn, A., & Marquart, T. 2021, *A&A*, 646, A32
- Piskunov, N. E. & Valenti, J. A. 2002, *A&A*, 385, 1095
- Pizzolato, N., Maggio, A., Micela, G., Sciortino, S., & Ventura, P. 2003, *A&A*, 397, 147
- Pont, F., Gilliland, R. L., Moutou, C., et al. 2007, *A&A*, 476, 1347
- Pont, F., Sing, D. K., Gibson, N. P., et al. 2013, *MNRAS*, 432, 2917
- Presca, A., Driessen, F. A., & Vidotto, A. A. 2024, *MNRAS*, 534, 3622
- Press, W. H., Teukolsky, S. A., Vetterling, W. T., & Flannery, B. P. 1992, *Numerical recipes in FORTRAN. The art of scientific computing*
- Rackham, B. V., Apai, D., & Giampapa, M. S. 2018, *ApJ*, 853, 122
- Rackham, B. V., Apai, D., & Giampapa, M. S. 2019, *AJ*, 157, 96
- Rees, D. E. & Semel, M. D. 1979, *A&A*, 74, 1
- Reiners, A., Shulyak, D., Käpylä, P. J., et al. 2022, *A&A*, 662, A41
- Reinhold, T. & Hekker, S. 2020, *A&A*, 635, A43
- Rusomarov, N., Kochukhov, O., Piskunov, N., et al. 2013, *A&A*, 558, A8
- Ryabchikova, T., Piskunov, N., Kurucz, R. L., et al. 2015, *Phys. Scr.*, 90, 054005
- Sachdeva, N., van der Holst, B., Manchester, W. B., et al. 2019, *ApJ*, 887, 83
- Salz, M., Czesla, S., Schneider, P. C., et al. 2018, *A&A*, 620, A97
- Saur, J., Grambusch, T., Duling, S., Neubauer, F. M., & Simon, S. 2013, *A&A*, 552, A119
- Schneider, E. M., Velázquez, P. F., Esquivel, A., Raga, A. C., & Blanco-Cano, X. 2007, *ApJ*, 671, L57
- Schrijver, C. J. & Zwaan, C. 2000, *Solar and Stellar Magnetic Activity*
- Semel, M. 1989, *A&A*, 225, 456
- Skilling, J. & Bryan, R. K. 1984, *MNRAS*, 211, 111
- Snik, F., Kochukhov, O., Piskunov, N., et al. 2011, in *Astronomical Society of the Pacific Conference Series*, Vol. 437, *Solar Polarization 6*, ed. J. R. Kuhn, D. M. Harrington, H. Lin, S. V. Berdyugina, J. Trujillo-Bueno, S. L. Keil, & T. Rimmele, 237
- Sokolov, I. V., van der Holst, B., Oran, R., et al. 2013, *ApJ*, 764, 23
- Spina, L., Nordlander, T., Casey, A. R., et al. 2020, *ApJ*, 895, 52
- Strugarek, A., Brun, A. S., Matt, S. P., & Réville, V. 2015, *ApJ*, 815, 111
- Strugarek, A., García Muñoz, A., Brun, A. S., & Paul, A. 2025, *A&A*, 693, A220
- Tessore, B., Lèbre, A., Morin, J., et al. 2017, *A&A*, 603, A129
- Tinetti, G., Drossart, P., Eccleston, P., et al. 2018, *Experimental Astronomy*, 46, 135
- Tinetti, G., Eccleston, P., Lueftinger, T., et al. 2022, in *European Planetary Science Congress. EPSC2022–1114*
- Torres, C. A. O., Quast, G. R., da Silva, L., et al. 2006, *A&A*, 460, 695
- Tóth, G., Sokolov, I. V., Gombosi, T. I., et al. 2005, *Journal of Geophysical Research (Space Physics)*, 110, A12226
- Tóth, G., van der Holst, B., Sokolov, I. V., et al. 2012, *Journal of Computational Physics*, 231, 870
- Tsantaki, M., Magrini, L., Danielski, C., et al. 2025, *A&A*, 697, A102
- van der Holst, B., Manchester, W. B., I., Klein, K. G., & Kasper, J. C. 2019, *ApJ*, 872, L18
- van der Holst, B., Sokolov, I. V., Meng, X., et al. 2014, *The Astrophysical Journal*, 782, 81
- van der Walt, S., Colbert, S. C., & Varoquaux, G. 2011, *Computing in Science and Engineering*, 13, 22
- Van Looveren, G., Boro Saikia, S., Herbot, O., et al. 2025, *A&A*, 694, A310
- Vidotto, A. A. 2025, *ARA&A*, 63, 299
- Vidotto, A. A., Bourrier, V., Fares, R., et al. 2023, *A&A*, 678, A152
- Vidotto, A. A. & Cleary, A. 2020, *MNRAS*, 494, 2417
- Vidotto, A. A., Fares, R., Jardine, M., et al. 2012, *MNRAS*, 423, 3285
- Vidotto, A. A., Fares, R., Jardine, M., Moutou, C., & Donati, J. F. 2015, *MNRAS*, 449, 4117
- Vidotto, A. A., Jardine, M., & Helling, C. 2010, *ApJ*, 722, L168
- Vidotto, A. A., Jardine, M., Morin, J., et al. 2014, *MNRAS*, 438, 1162
- Vidotto, A. A., Lichtenegger, H., Fossati, L., et al. 2018, *MNRAS*, 481, 5296
- Vidotto, A. A., Opher, M., Jatenco-Pereira, V., & Gombosi, T. I. 2009, *ApJ*, 703, 1734
- Villarreal D'Angelo, C., Esquivel, A., Schneider, M., & Sgró, M. A. 2018, *MNRAS*, 479, 3115
- Virtanen, P., Gommers, R., Burovski, E., et al. 2020, *scipy/scipy: SciPy 1.5.3*
- Willamo, T., Lehtinen, J. J., Hackman, T., et al. 2022, *A&A*, 659, A71
- Zingales, T., Tinetti, G., Pillitteri, I., et al. 2018, *Experimental Astronomy*, 46, 67

Appendix A: Additional figures

In this appendix we provide the observed Stokes V LSD profiles used for the ZDI reconstruction and their Unno-Rachkovsky models. Fig. A.1 shows the Stokes V LSD profiles for TOI-1860, DS Tuc A, and HD 63433 analysed in this work.

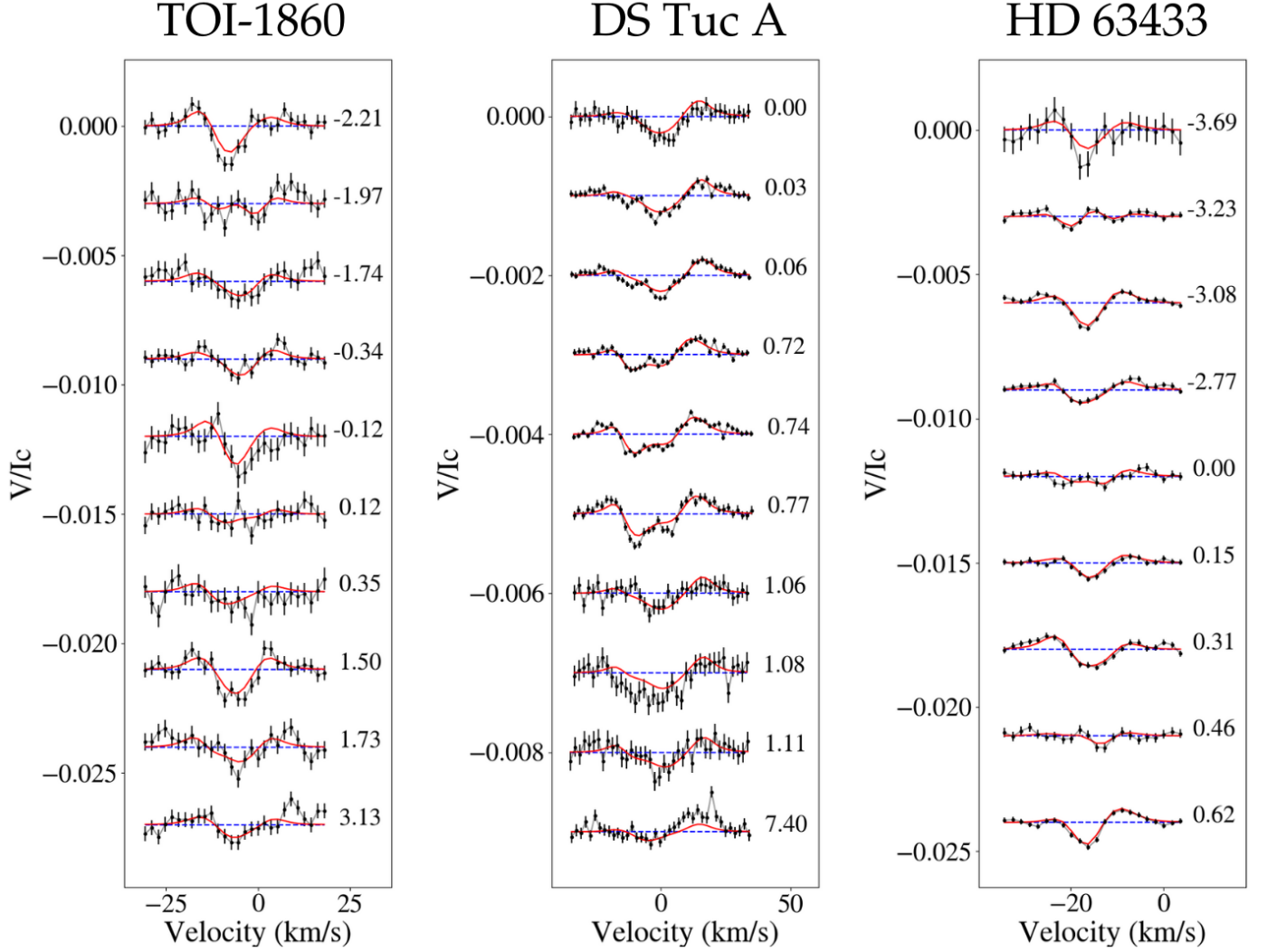


Fig. A.1. Time series of Stokes V LSD profiles and the ZDI models for TOI-1860, DS Tuc A, and HD 63433. The observations are shown in black and the models in red. The numbers on the right indicate the rotational cycle computed from Eq. 3 using the first observation of an epoch as reference date for DS Tuc A and the median observation for TOI-1860 and HD 63433. The horizontal line represents the zero point of the profiles, which are shifted vertically based on their rotational phase for visualisation purposes.

Appendix B: Journal of observations

In this appendix, we provide a list of the observations performed with Neo-Narval, HARPSpol, and SPIRou. We also list the value of the longitudinal magnetic field (B_ℓ).

Table B.1. Journal of observations

Star	Instrument	Date [yyyy-mm-dd]	UT [hh:mm:ss]	HJD [-2450000]	t_{exp} [s]	S/N	FAP _V	Detection _V	$\sigma_{\text{LSD,V}}$ [$10^{-4}I_c$]	B_ℓ [G]	FAP _N	Detection _N	$\sigma_{\text{LSD,N}}$ [$10^{-4}I_c$]
HD 63433	Neo-Narval	2024-03-18	20:51:40.58	10388.3679	4x883	326	1.80E-01	ND	2.41	-0.9 ± 8.0	9.94E-01	ND	2.7
HD 63433	Neo-Narval	2024-03-21	20:54:30.59	10391.3695	4x883	505	1.52E-06	D	1.10	-0.9 ± 2.1	6.52E-01	ND	1.03
HD 63433	Neo-Narval	2024-03-22	20:03:28.64	10392.3340	4x883	605	0.00E-00	D	1.25	0.0 ± 1.6	9.76E-01	ND	0.85
HD 63433	Neo-Narval	2024-03-24	20:44:58.99	10394.3626	4x883	527	0.00E-00	D	1.09	-4.4 ± 1.9	6.33E-01	ND	0.98
HD 63433	Neo-Narval	2024-04-11	19:58:43.77	10412.3290	4x883	408	4.86E-02	ND	1.37	-2.9 ± 2.6	9.47E-01	ND	1.27
HD 63433	Neo-Narval	2024-04-12	19:33:13.52	10413.3112	4x883	578	0.00E-00	D	0.98	-3.1 ± 1.7	4.14E-02	ND	0.88
HD 63433	Neo-Narval	2024-04-13	19:48:49.81	10414.3219	4x883	488	0.00E-00	D	1.26	5.0 ± 1.9	2.11E-01	ND	1.00
HD 63433	Neo-Narval	2024-04-14	20:21:20.89	10415.3444	4x883	396	2.43E-02	ND	1.32	3.3 ± 2.8	6.67E-01	ND	1.39
HD 63433	Neo-Narval	2024-04-15	20:01:09.13	10416.3304	4x883	552	0.00E-00	D	1.19	-5.7 ± 1.6	9.92E-01	ND	0.80
HD 63935	Neo-Narval	2023-11-19	03:28:06.76	10267.6497	4x898	243	1.00E-01	ND	2.81	< 30	3.70E-01	ND	2.87
HD 63935	Neo-Narval	2023-11-20	03:19:59.39	10268.6441	4x898	234	6.53E-01	ND	2.48	< 32	6.48E-01	ND	2.70
HD 63935	Neo-Narval	2023-11-26	03:30:11.50	10274.6514	4x898	243	1.00E+00	ND	3.15	< 50	9.84E-01	ND	3.27
HD 63935	Neo-Narval	2024-01-10	00:23:49.40	10319.5213	4x898	243	6.82E-01	ND	2.39	< 30	4.13E-01	ND	2.56
HD 63935	HARPSpol	2022-12-24	05:05:10.35	9937.7169	4x900	295	9.38E-01	ND	1.68	< 20	5.34E-01	ND	1.71
HD 63935	HARPSpol	2022-12-26	04:27:45.35	9939.6910	4x900	190	9.76E-02	ND	2.22	< 20	6.35E-02	ND	2.07
HD 63935	HARPSpol	2023-02-06	04:54:38.00	9981.7099	4x900	220	6.90E-01	ND	1.37	< 270	2.56E-01	ND	1.53
HD 63935	HARPSpol	2023-02-07	03:36:16.32	9982.6554	4x900	310	9.99E-01	ND	1.71	< 110	9.99E-01	ND	1.67
HD 89345	Neo-Narval	2024-01-10	03:37:48.25	10319.6570	4x868	5	9.56E-01	ND	49.72	< 800	9.88E-01	ND	48.74
HD 89345	Neo-Narval	2024-01-13	03:48:17.25	10322.6642	4x868	152	8.77E-01	ND	2.75	< 30	7.05E-01	ND	2.58
HD 89345	Neo-Narval	2024-01-20	02:45:43.64	10329.6208	4x868	73	4.59E-01	ND	8.36	< 120	5.28E-01	ND	8.15
HD 89345	Neo-Narval	2024-01-27	02:17:24.19	10336.6010	4x868	56	2.41E-01	ND	8.21	< 100	2.75E-02	ND	8.26
HD 89345	Neo-Narval	2024-02-18	02:44:54.32	10358.6192	4x868	45	3.07E-02	ND	17.94	< 230	4.71E-03	MD	16.81
HD 152843	Neo-Narval	2023-09-24	18:46:43.76	10212.2787	4x846	111	4.11E-01	ND	5.74	< 90	9.45E-01	ND	4.64
HD 152843	Neo-Narval	2023-10-02	19:06:31.76	10220.2923	4x846	21	2.91E-01	ND	24.73	< 350	1.60E-02	ND	25.67
HD 152843	Neo-Narval	2023-10-03	18:45:57.52	10221.2779	4x846	143	9.47E-01	ND	3.65	< 50	7.03E-01	ND	3.57
HD 158259	Neo-Narval	2023-09-05	19:15:13.11	10193.3012	4x893	413	6.81E-01	ND	1.49	< 9	1.44E-02	ND	1.39
HD 158259	Neo-Narval	2023-09-10	19:40:16.58	10198.3186	4x893	689	1.53E-01	ND	0.78	< 5	9.98E-01	ND	0.84
HD 158259	Neo-Narval	2023-09-23	19:13:46.56	10211.3000	4x893	482	4.16E-01	ND	1.14	< 7	9.43E-01	ND	1.24
HD 260655	SPIRou	2024-03-03	05:06:56.37	10372.7118	4x1203	222	9.29E-01	ND	2.81	< 130	8.98E-01	ND	2.32
HAT-P-22	Neo-Narval	2024-03-12	23:12:19.17	10382.4681	4x1207	45	8.47E-01	ND	8.75	< 50	2.28E-01	ND	9.76
HAT-P-22	Neo-Narval	2024-03-13	23:22:33.80	10383.4751	4x1207	102	5.16E-02	ND	10.16	< 50	4.11E-01	ND	9.70
DSTuc	HARPSpol	2025-07-18	05:01:41.36	10874.7477	4x1499	385	1.66E-04	MD	0.63	-11.4 ± 8.7	1.00E-00	ND	0.48
DSTuc	HARPSpol	2025-07-18	07:14:14.59	10874.8399	4x1499	437	0.00E-00	D	0.59	-16.9 ± 4.1	9.71E-01	ND	0.38
DSTuc	HARPSpol	2025-07-18	08:57:30.59	10874.9116	4x1499	372	0.00E-00	D	0.61	-19.4 ± 3.5	7.57E-01	ND	0.38
DSTuc	HARPSpol	2025-07-20	06:10:29.01	10876.7955	4x1499	359	0.00E-00	D	0.53	-21.3 ± 3.6	7.80E-01	ND	0.37
DSTuc	HARPSpol	2025-07-20	07:53:27.62	10876.8670	4x1499	419	0.00E-00	D	0.63	-29.1 ± 3.2	3.73E-01	ND	0.39
DSTuc	HARPSpol	2025-07-20	09:36:14.21	10876.9314	4x1199	351	0.00E-00	D	0.75	-21.8 ± 5.0	9.96E-01	ND	0.42
DSTuc	HARPSpol	2025-07-21	05:28:24.27	10877.7663	4x1499	164	8.30E-02	ND	0.95	-11.4 ± 9.1	4.02E-01	ND	0.90
DSTuc	HARPSpol	2025-07-21	07:11:36.07	10877.8379	4x1499	232	2.77E-05	D	1.10	-21.6 ± 11.7	5.20E-01	ND	0.96

Table B.1. continued.

Star	Instrument	Date [yyyy-mm-dd]	UT [hh:mm:ss]	HJD [-2450000]	t_{exp} [s]	S/N	FAP _V	Detection _V	$\sigma_{\text{LSD,V}}$ [$10^{-4}I_c$]	B_ℓ [G]	FAP _N	Detection _N	$\sigma_{\text{LSD,N}}$ [$10^{-4}I_c$]
DS Tuc	HARSPol	2025-07-21	08:54:19.49	10877.9093	4x1499	162	4.07E-02	ND	1.00	-4.4 ± 11.7	9.27E-01	ND	0.92
DS Tuc	HARSPol	2025-08-08	07:05:44.15	10895.8333	4x1499	349	1.68E-13	D	0.79	-36.3 ± 6.8	6.71E-03	MD	0.67
Kepler-444	Neo-Narval	2023-09-20	20:24:00.13	10208.3498	4x857	166	3.85E-01	ND	2.19	< 40	9.84E-01	ND	2.07
Kepler-444	Neo-Narval	2023-09-23	20:20:22.85	10211.3472	4x857	162	9.25E-01	ND	2.43	< 43	5.29E-01	ND	2.50
Kepler-444	Neo-Narval	2023-09-24	20:24:17.13	10212.3499	4x857	154	5.26E-01	ND	2.77	< 60	5.31E-01	ND	2.55
Kepler-444	Neo-Narval	2023-10-02	20:19:47.91	10220.3464	4x857	100	5.33E-01	ND	5.92	< 110	6.09E-01	ND	5.28
K2-116	SPiRou	2023-07-01	10:38:27.93	10126.9490	4x902	285	2.52E-01	ND	0.94	< 12	1.03E-01	ND	0.96
K2-116	SPiRou	2023-07-26	14:20:44.47	10152.1035	4x902	272	1.60E-01	ND	1.07	< 14	2.52E-01	ND	1.04
K2-116	SPiRou	2023-10-03	05:00:18.87	10220.7100	4x902	235	9.90E-01	ND	1.14	< 13	7.05E-01	ND	1.26
TOI-836	SPiRou	2024-03-15	12:45:53.35	10385.0374	4x1203	76	9.30E-03	MD	27.59	62 ± 190	1.22E-05	D	33.57
TOI-1136	Neo-Narval	2024-03-13	00:38:36.67	10382.5280	4x896	108	2.76E-01	ND	3.27	< 42	2.89E-01	ND	3.32
TOI-1136	Neo-Narval	2024-03-14	00:52:55.94	10383.5379	4x896	79	1.13E-01	ND	11.93	< 70	2.00E-01	ND	10.79
TOI-1136	Neo-Narval	2024-03-16	23:28:46.44	10386.4793	4x896	17	1.68E-04	MD	54.71	120 ± 106	2.87E-07	D	59.52
TOI-1136	Neo-Narval	2024-03-18	23:03:40.12	10388.4618	4x896	22	1.52E-04	MD	36.69	25 ± 44	6.73E-04	MD	34.77
TOI-1136	Neo-Narval	2024-03-19	21:26:21.83	10389.3942	4x896	17	1.63E-05	D	49.39	131 ± 60	1.11E-03	MD	45.71
TOI-1136	Neo-Narval	2024-03-21	22:49:35.78	10391.4519	4x896	103	3.38E-01	ND	3.68	< 52	1.19E-01	ND	3.72
TOI-1860	Neo-Narval	2024-03-25	01:18:49.96	10394.5557	4x881	91	3.31E-02	ND	3.38	-0.4 ± 8.1	2.81E-02	ND	3.54
TOI-1860	Neo-Narval	2024-04-12	00:11:05.63	10412.5082	4x881	139	9.04E-03	MD	2.32	-2.0 ± 5.8	2.92E-02	ND	2.32
TOI-1860	Neo-Narval	2024-04-14	00:59:00.79	10414.5414	4x881	222	3.79E-02	ND	3.81	10.3 ± 10.4	7.73E-01	ND	3.81
TOI-1860	Neo-Narval	2024-04-16	01:48:11.36	10416.5755	4x881	256	1.51E-03	MD	5.57	6.9 ± 12.9	9.87E-01	ND	5.14
TOI-1860	Neo-Narval	2024-08-09	20:15:41.51	10532.3425	4x881	186	4.06E-01	ND	3.03	-3.0 ± 8.2	3.05E-01	ND	3.32
TOI-1860	Neo-Narval	2024-08-15	20:10:07.52	10538.3386	4x881	197	4.63E-01	ND	3.75	4.6 ± 9.7	4.73E-01	ND	3.84
TOI-1860	Neo-Narval	2025-06-29	21:34:18.71	10856.3973	4x881	268	1.98E-03	MD	5.28	18.7 ± 14.4	4.37E-01	ND	4.98
TOI-1860	Neo-Narval	2025-06-30	21:54:41.27	10857.4114	4x881	229	2.24E-13	D	3.30	-4.5 ± 6.6	1.86E-01	ND	2.66
TOI-1860	Neo-Narval	2025-07-01	22:09:10.24	10858.4215	4x881	218	5.19E-09	D	3.00	10.4 ± 6.5	1.23E-02	ND	2.46
TOI-1860	Neo-Narval	2025-07-07	22:20:38.77	10864.4293	4x881	294	4.45E-02	ND	3.66	-8.5 ± 8.5	4.74E-01	ND	3.51
TOI-1860	Neo-Narval	2025-07-15	21:36:13.20	10872.3984	4x881	242	4.81E-01	ND	12.41	31.3 ± 31.3	7.62E-01	ND	11.32
TOI-1860	Neo-Narval	2025-07-16	21:30:44.22	10873.3946	4x881	218	7.77E-16	D	2.95	-2.8 ± 6.4	4.35E-01	ND	2.43
TOI-1860	Neo-Narval	2025-07-22	21:40:37.13	10879.4014	4x881	278	1.66E-02	ND	3.10	-13.0 ± 8.3	9.92E-01	ND	2.76
TOI-1860	Neo-Narval	2025-07-08	22:05:04.57	10865.4185	4x881	188	2.89E-12	D	3.05	2.3 ± 6.6	6.62E-01	ND	2.48
TOI-1860	Neo-Narval	2025-07-09	21:57:32.90	10866.4133	4x881	233	5.71E-03	MD	3.12	19.4 ± 8.0	9.32E-01	ND	3.19
TOI-1860	Neo-Narval	2025-07-10	22:10:26.97	10867.4222	4x881	224	1.29E-03	MD	2.70	-20.5 ± 6.4	5.78E-01	ND	2.52
TOI-1860	Neo-Narval	2025-08-15	20:01:16.85	10903.3325	4x881	115	3.76E-05	D	5.82	-8.5 ± 8.0	9.76E-01	ND	4.93
TOI-1860	Neo-Narval	2025-08-16	20:00:36.42	10904.3320	4x881	133	5.29E-01	ND	2.75	-43.5 ± 19.3	8.78E-01	ND	2.59
TOI-1860	Neo-Narval	2025-08-17	20:00:12.42	10905.3318	4x881	140	4.27E-01	ND	2.49	-19.8 ± 15.4	2.31E-01	ND	2.43
TOI-1860	Neo-Narval	2025-08-23	19:54:42.98	10911.3280	4x881	203	8.95E-01	ND	1.33	-4.4 ± 9.2	6.44E-01	ND	1.32
TOI-2076	Neo-Narval	2024-01-20	05:31:37.14	10329.7332	4x900	97	2.45E-01	ND	4.70	< 98	9.97E-01	ND	4.56
TOI-2076	Neo-Narval	2024-01-26	05:01:18.48	10335.7124	4x900	160	2.90E-02	MD	2.67	-75 ± 17	4.49E-01	ND	3.45
TOI-2076	Neo-Narval	2024-02-18	04:48:15.35	10358.7038	4x900	101	1.73E-03	ND	6.40	< 102	9.45E-01	ND	6.02
TOI-2076	Neo-Narval	2024-03-22	01:51:51.71	10391.5810	4x851	104	7.55E-03	MD	6.84	69 ± 34	5.07E-02	ND	6.59
TOI-2076	Neo-Narval	2024-03-25	00:16:05.50	10394.5144	4x851	85	6.20E-01	ND	5.31	< 150	9.55E-01	ND	5.63
TOI-2076	Neo-Narval	2024-04-11	23:06:52.55	10412.4657	4x851	87	3.12E-01	ND	8.80	< 93	5.83E-01	ND	9.08
Wolf 503	SPiRou	2023-07-24	06:13:55.10	10149.7558	4x902	324	7.27E-01	ND	37.13	< 25	8.50E-01	ND	42.32

Table B.1. continued.

Star	Instrument	Date [yyyy-mm-dd]	UT [hh:mm:ss]	HJD [-2450000]	t_{exp} [s]	S/N	FAP _V	Detection _V	$\sigma_{\text{LSD},V}$ [$10^{-4}I_c$]	B_ℓ [G]	FAP _N	Detection _N	$\sigma_{\text{LSD},N}$ [$10^{-4}I_c$]
Wolf 503	SPIrou	2024-03-01	13:15:28.64	10371.0582	4x1203	156	8.78E-01	ND	0.51	< 190	9.96E-01	ND	0.48
Wolf 503	SPIrou	2024-03-15	11:06:41.78	10384.9687	4x1203	61	3.68E-01	ND	5.71	< 500	3.19E-01	ND	5.68

The following quantities are listed: star identifier, instrument used for the observations, date and time of the observation, Heliocentric Julian date, exposure time per polarimetric sequence, S/N per polarimetric sequence at 650 nm (for Neo-Narval and HARPSpol) or at 1650 nm (for SPIrou) per resolution pixel, false-alarm probability for Stokes V detection, status of Stokes V detection (D = detection, MD = marginal detection and ND = non-detection), RMS noise level of Stokes V signal in units of unpolarised continuum, longitudinal magnetic field or 3σ upper limit computed using Eq. 1, false-alarm probability for Stokes N detection, status of Stokes N detection, and RMS noise level of Stokes N signal in units of unpolarised continuum.